

Remote Sensing of Environment

Estimating Urban Sensible Heat Flux Using GOES-16 Satellite Data

--Manuscript Draft--

Manuscript Number:	RSE-D-21-00397
Article Type:	Research Paper
Section/Category:	Land surface energy and water balance
Keywords:	Sensible Heat Flux; Urban; Satellite Remote Sensing; GOES-16; Atmospheric Modeling; Boundary Layer; National Land Cover Database
Corresponding Author:	Gabriel Rios City College of the City University of New York: The City College of New York UNITED STATES
First Author:	Gabriel Rios
Order of Authors:	Gabriel Rios Prathap Ramamurthy, PhD
Abstract:	A model for calculating sensible heat flux (Q_H) – a primary component of the urban surface energy budget – is presented here. Remote sensing data from the NASA/NOAA GOES-16 satellite and a high-resolution land cover dataset are used as inputs to estimate the spatiotemporal variability of Q_H in urban areas. The primary motivation for this model is to present a cost-effective approach to calculate Q_H independent of traditional flux observations and computational methods. The GOES-16 satellite data, which has a moderate spatial and high temporal resolution (2 km square at 5 minute intervals) enables the estimation of Q_H over highly heterogeneous urban areas. The model is constructed using an iterative algorithm that uses a surface layer turbulence parameterization to solve for Q_H as a function of the enterprise GOES-16 Land Surface Temperature product, an urban air temperature model, publicly-accessible ground observations, and the National Land Cover Database (NLCD). Model validation was performed over a year-long period spanning from 2019 June to 2020 May. Three (3) ground flux stations within New York City located in areas with varying degrees of urbanization were used for model validation. Statistics from validation studies found an RMSE of 44.6 W-m ⁻² , a mean bias error of 12.4 W-m ⁻² , and a R ² of 0.71. Validation results demonstrate that the algorithm shows good correlation with observed values, suggesting that satellite data can be used as an accessible and cost-effective option to estimate Q_H in urban areas. The satellite-based model outperformed conventional high-resolution urban numerical model.
Suggested Reviewers:	Jonathan Munoz Barreto, PhD University of Puerto Rico Mayaguez: Recinto Universitario de Mayaguez Universidad de Puerto Rico jonathan.munoz@upr.edu
	Fredrik Lindberg Researcher, University of Gothenburg: Goteborgs Universitet fredrikl@gvc.gu.se
	Benjamin Crawford, PhD Assistant Professor, University of Colorado Denver benjamin.crawford@ucdenver.edu
Opposed Reviewers:	

- Novel method uses remote sensing data for estimation of urban sensible heat flux
- Model and observations agree within $45 \text{ W}\cdot\text{m}^{-2}$ with bias of $12.4 \text{ W}\cdot\text{m}^{-2}$ over study period
- Outperformance of Weather Research Forecasting model during study period
- Model uses open-access data (e.g. GOES-16) for cost-effective performance

[Click here to view linked References](#)

1 Estimating Urban Sensible Heat Flux Using GOES 16 Satellite 2 Data

3 Gabriel Rios^{*1, 2} and Prathap Ramamurthy^{1, 2}

4 ¹Department of Mechanical Engineering, CUNY City College, New York, NY 10031, USA

5 ²NOAA CREST Center, CUNY City College, New York, NY 10031, USA

6 Abstract

7 A model for calculating sensible heat flux (Q_H) – a primary component of the urban surface energy
8 budget – is presented here. Remote sensing data from the NASA/NOAA GOES-16 satellite and a high-
9 resolution land cover dataset are used as inputs to estimate the spatiotemporal variability of Q_H in urban
10 areas. The primary motivation for this model is to present a cost-effective approach to calculate Q_H
11 independent of traditional flux observations and computational methods. The GOES-16 satellite data,
12 which has a moderate spatial and high temporal resolution (2 km square at 5 minute intervals) enables
13 the estimation of Q_H over highly heterogeneous urban areas. The model is constructed using an iterative
14 algorithm that uses a surface layer turbulence parameterization to solve for Q_H as a function of the enter-
15 prise GOES-16 Land Surface Temperature product, an urban air temperature model, publicly-accessible
16 ground observations, and the National Land Cover Database (NLCD). Model validation was performed
17 over a year-long period spanning from 2019 June to 2020 May. Three (3) ground flux stations within New
18 York City located in areas with varying degrees of urbanization were used for model validation. Statistics
19 from validation studies found an RMSE of 44.6 W m^{-2} , a mean bias error of 12.4 W m^{-2} , and a R^2 of
20 0.71. Validation results demonstrate that the algorithm shows good correlation with observed values,
21 suggesting that satellite data can be used as an accessible and cost-effective option to estimate Q_H in ur-
22 ban areas. The satellite-based model outperformed conventional high-resolution urban numerical model.

23
24 *Keywords:* Sensible Heat Flux, Urban, Satellite Remote Sensing, GOES-16, Atmospheric Modeling,
25 GOES-16, National Land Cover Database

26
27 **Corresponding author:* Gabriel Rios, Department of Mechanical Engineering, CUNY City College,
28 New York, NY 10031, USA. E-mail: grios001@citymail.cuny.edu

30 1 Introduction and Background

31 Sensible heat flux (Q_H) is a key component of the Earth's surface energy balance, as it characterizes the
32 surface-to-atmosphere transport of heat. In urban environments, Q_H is the most critical term due to the
33 anthropogenic modification of land cover, which increases heat storage as opposed to water retention. Q_H in
34 cities impacts the urban heat island dynamics, hence, it has significant implications on weather prediction and
35 forecasting, air pollution, and building energy use. (Vautard et al. (2007), Imran et al. (2018), Schumacher
36 et al. (2019)).

37 Q_H is driven by a number of factors - particularly the temperature difference between the land surface
38 temperature (LST) and the air temperature (T_{air}) in the lowest levels of the boundary layer. The LST

39 has been shown to be higher in urban areas than surrounding suburban/rural areas ([Price \(1979\)](#)), which
40 is driven by the heterogeneity in urban land cover and its constituent materials. The increased LST can
41 both increase T_{air} and the temperature difference between the two, resulting in an increased Q_H relative to
42 surrounding areas ([Kato & Yamaguchi \(2005\)](#)).

43 A challenge in understanding the relationship between land cover, LST, T_{air} and Q_H is presented by the
44 techniques used for measurement and estimation of Q_H . This challenge is brought about by a number of
45 factors, including (but not limited to):

- 46 • Computationally-expensive numerical models for estimation purposes ([Best \(2005\)](#), [Zhang et al. \(2015\)](#)),
47 and
- 48 • The lack of well-established measurement networks in rural and urban areas ([Voogt & Oke \(2003\)](#),
49 [Chrysoulakis et al. \(2018\)](#))

50 Numerical models are powerful estimation tools that allow for the understanding of atmospheric processes
51 at much greater extents than possible by measurement and observation alone. However, these models can
52 often feature significant inaccuracies in areas with high spatial heterogeneity, such as urban areas, due to
53 low grid domain resolutions relative to the size and spacing of elements in heterogeneous environments (e.g.
54 buildings, roads, scattered green space and vegetative cover) ([Chen et al. \(2011\)](#), [Hong & Dudhia \(2012\)](#),
55 [Leroyer et al. \(2014\)](#)). Accordingly, it is often that model accuracy can only be improved upon by significantly
56 increasing model resolution to resolve these spatial issues, which risks high time and resource consumption.

57 Regarding measurement networks, observational data is an essential source of validation data for numerical
58 models to ensure their performance. However, accurate measurement of parameters, such as Q_H , is
59 challenged by the lack of measurement networks with sufficient spatial resolution that can serve as databases
60 for validation efforts. Moreover, this challenge is exacerbated in urban areas due to the aforementioned land
61 cover heterogeneity, which is critical in determining Q_H in localized areas ([Feddem et al. \(2005\)](#), [Wang
et al. \(2016\)](#)). To address this, remote sensing technologies have been increasingly used to devise estimation
63 methods for Q_H ([Stewart et al. \(1994\)](#), [Voogt & Grimmond \(2000\)](#), [Nadeau et al. \(2009\)](#), [Kim & Kwon
\(2019\)](#)).

65 Numerous studies detailing methods for the estimation of Q_H in rural and urban areas using remote
66 sensing technologies have been successfully performed. For rural areas, [Stewart et al. \(1994\)](#) described the
67 use of radiometers for measurement of an arid valley in California and [Kim & Kwon \(2019\)](#) demonstrated
68 the use of unmanned aerial vehicles (UAV) to collect data over a range of areas featuring varying land
69 cover types. In urban areas, [Voogt & Grimmond \(2000\)](#) implemented a method for estimating Q_H over a
70 400 x 300 m sector of Vancouver using a helicopter-mounted thermal scanner for surface temperature data
71 collection and [Nadeau et al. \(2009\)](#) evaluated heat fluxes over a 400 x 300 m sector of an urban area using
72 a dense network of weather stations and a scintillometer. Despite the considerable agreement between the
73 presented estimation methods and the corresponding observed data, all are limited by spatiotemporal extent
74 (e.g. geographic extent limited to several city blocks, data collection periods limited to a few days) and/or
75 expensive methods for data collection, which can hinder the validation of the estimation method over a range
76 of factors, such as spatial variability due to heterogeneous land cover and temporal variability due to daily
77 or seasonal changes in atmospheric conditions.

78 In this study, a method for estimating Q_H using a combination of open-access remote sensing and
79 ground observational data in a dedicated, cost-effective satellite-based model is introduced. The objective
80 of this method is to use satellite data to provide a large spatial and temporal domain over which Q_H

81 can be accurately estimated. The model uses satellite data from the NOAA/NASA Geostationary Oper-
82 ational Environmental Satellite (GOES-16), ground observational data from NWS/FAA/DOD Automated
83 Surface Observing Systems (ASOS) stations, and land cover data from the MRLC 2016 National Land Cover
84 Database (NLCD) to estimate Q_H .

85 The primary advantage to using the GOES-16 satellite for the estimation of Q_H is the spatial extent
86 and high temporal resolution of its collected data. These properties provide a basis for a robust validation
87 process for the model, increasing confidence in its accuracy. Although GOES-16 satellite data features some
88 limitations such as inability to reliably estimate during periods with significant sky cover and a moderate
89 spatial resolution of 2 km, the benefits provided by remote sensing data for Q_H estimation allow for the
90 limitations of previous studies with similar objectives to be addressed and mitigated.

91 The primary objectives of this paper are:

- 92 • To develop a satellite-based model to estimate the Q_H of urban environments at high temporal and
93 moderate spatial resolutions.
- 94 • To validate and compare the satellite-based estimates of Q_H with ground-based observations, as well as
95 with Q_H derived from high-resolution urban climate models, both temporally and spatially for multiple
96 seasons.

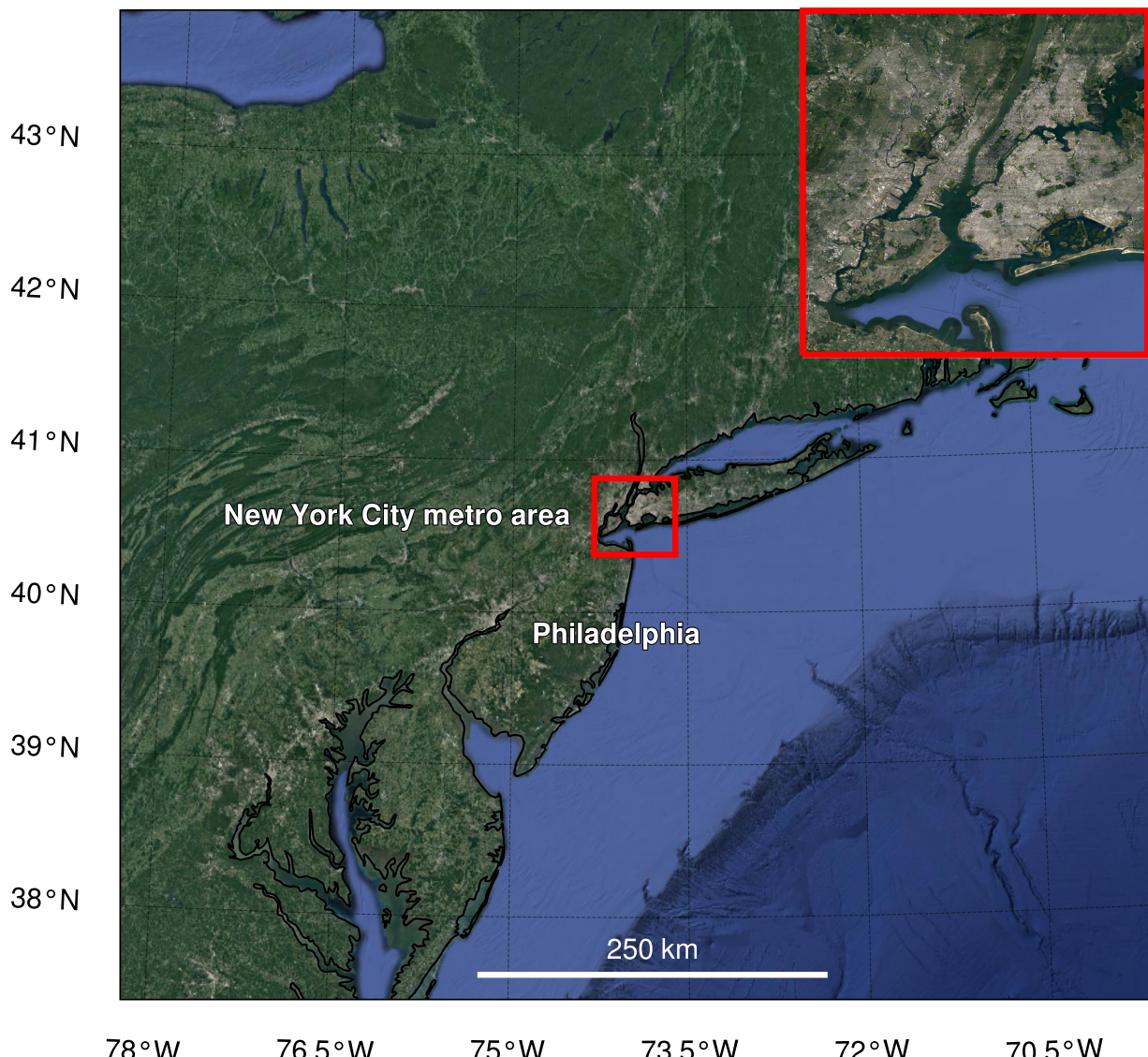


Figure 1: Satellite view of the mid-Atlantic and northeastern United States. The study area is outlined by the red frame, which can be seen in greater detail in the inset.

97 This study focuses on New York City (see Figure 1), which is the largest city in the United States
98 by population, with approximately 8.3 million people as of 2019 ([Bureau \(2019\)](#)) and is among the most

99 densely-populated cities in the United States. The city, which spans a total land area of 778 km^2 (Bureau
100 (2019)), features a highly varied array of land cover types, spanning from open water (Hudson and East
101 Rivers, New York Bay) to highly-developed urban areas with numerous buildings exceeding 180 m in height
102 (Manhattan and Brooklyn) to deciduous forest (Staten Island woodlands and Van Cortlandt Park in the
103 Bronx). The complex urban landscape, coupled with an array of urban flux towers and weather observation
104 stations within the city, make the city an ideal candidate for implementing and validating the urban-focused
105 Q_H model.

106 This paper will first discuss the theoretical background for the satellite model, including the usage of
107 Monin-Obukhov similarity theory Monin & Obukhov (1954) and the methodology for estimation of element
108 roughness heights in urban areas. Next, the paper reviews the use of GOES-16 satellite data and an associated
109 urban air temperature model (Hrisko et al. (2020)) as inputs in the model, as well as how ground stations
110 were used for model inputs and validation. Subsequently, the model results over the year-long study period
111 are presented, along with validation data accompanied by a statistical evaluation of model performance
112 against ground stations. Finally, there is a discussion regarding the performance of the model, potential
113 sources of error within the model and the validation process, as well as application potential and future work
114 to improve the methods presented here.

115 2 Methodology and Data

116 2.1 Sensible Heat Flux Iterative Algorithm

117 Q_H is determined using a bulk turbulence parameterization based on scaling arguments presented by Monin-
118 Obukhov similarity theory (MOST) (Monin & Obukhov (1954)). The algorithm is dependent on the con-
119 vergence of Q_H , which in turn is dependent on the Obukhov length (L), as is the case in other algorithms
120 found in the literature (Launiainen & Vihma (1990), Grimmond & Cleugh (1994)). An assumption of a
121 convectively-stable atmosphere ($L \rightarrow \infty$) defines initial conditions for the model. Momentum and thermal
122 stability parameters, ψ_m and ψ_h , are approximately 0 at this initial condition. The following static and
123 dynamic variables - momentum and thermal roughness heights z_m and z_T , the bulk heat transfer coefficient
124 C_H , the friction velocity u^* , the Obukhov length L , and ultimately, Q_H are calculated by iteration, similar
125 to land surface models. Convergence is defined by a $<1\%$ change in Q_H between iterations. A flowchart of
126 the model structure is shown in Figure 2.

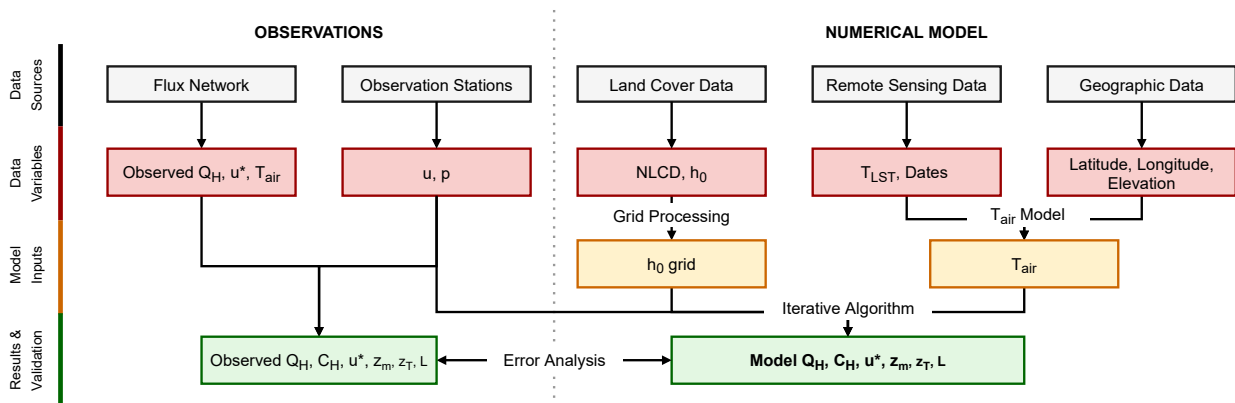


Figure 2: Process flowchart for the sensible heat flux model. Observational data was used for validation of the satellite model.

127 Q_H is calculated using Equation 1 (Pond et al. (1974)):

$$Q_H = \rho c_p C_H u (\theta_0 - \theta_r) \quad (1)$$

In Equation 1, ρ is air density calculated as a function of air pressure (p) and air temperature at the reference height of 2 m above ground level (AGL) (T_{air}), c_p is the average specific heat of air (1006 J $kg^{-1}K^{-1}$) across the range of air temperatures and pressures observed, C_H is a bulk heat transfer coefficient, u is the observed wind speed at a height of 10 m AGL, and θ_0 and θ_r are potential temperatures at the surface and at 2 m AGL, respectively.

C_H is calculated using Equation 2 (Monin & Obukhov (1954)):

$$C_H = \frac{\kappa^2}{[\ln \frac{z_r}{z_m} - \psi_m \zeta][\ln \frac{z_r}{z_T} - \psi_h \zeta]} \quad (2)$$

In Equation 2, κ is the von Karman constant (assumed to be 0.4), z_r is the reference height of measurement, z_m is the momentum roughness height, z_T is the thermal roughness height, ψ_m and ψ_h are the momentum and thermal stability parameters, respectively (Businger et al. (1971), Dyer (1974)), and ζ is an atmospheric stability parameter, defined as $\zeta = \frac{z_r}{L}$.

The roughness heights, z_m and z_T , are calculated using the Raupach [Equation 3] and Zilitinkevich [Equation 5] methods, respectively. The Raupach method (Raupach (1994)) for defining the momentum roughness height has been found useful in areas with heterogeneous land cover, as the roughness height can be calculated as a function of localized parameters and atmospheric conditions, specifically canopy height h_0 and local friction velocity u^* (Voogt & Grimmond 2000). The Zilitinkevich method has been shown to be an effective approximation method for z_T in areas with tall canopies, such as those present in urban areas, while enabling z_T to be calculated as a function of local parameters (Zilitinkevich (1995) Chen & Zhang (2009)), as described in Li & Bou-Zeid (2014).

$$z_m = h_0(1 - \frac{z_d}{h_0}) \exp[-\kappa \frac{u}{u^*} + 0.193] \quad (3)$$

where:

$$z_d = \exp[0.9793 * \ln(h_0) - 0.1536] \quad (4)$$

$$z_T = z_m \exp[-\kappa C_{zil} \sqrt{Re_t}] \quad (5)$$

where:

$$C_{zil} = 10^{-0.4*h_0} \quad (6)$$

$$Re_t = \frac{z_m u^*}{\nu} \quad (7)$$

The friction velocity u^* is expressed by Equation 5 (Monin & Obukhov (1954)):

$$u^* = \frac{\kappa u}{\ln \frac{z}{z_m} - \psi_m \zeta} \quad (8)$$

The Obukhov length L is expressed by Equation 6 (Monin & Obukhov (1954)):

$$L = \frac{-\rho c_p (u^*)^3 (\theta_0 + \theta_r)}{2 \kappa g Q_H} \quad (9)$$

The iterative model typically converged within 5 iterations, with convergence having been somewhat dependent on atmospheric stability ζ - the more unstable the atmosphere, the more difficulty the model had in converging.

154 2.2 Roughness Height Calculation Algorithm

155 The roughness height (h_0) describes the height of objects that protrude from the surface, such as buildings
 156 or trees. The roughness heights are calculated using a weighted average consisting of land cover parameters
 157 from the 2016 National Land Cover Database (NLCD) (Yang et al. 2018) and roughness heights from values
 158 specific to urban areas from the Weather Research Forecasting (WRF) model (Skamarock et al. 2008).

159 The NLCD data features 20 land cover classes, each with different roughness heights. The NLCD data is
 160 packaged in a 30 x 30 m grid spanning the continental United States (CONUS) and Alaska. To match the
 161 2 x 2 km gridded data presented by the GOES-16 LST product, the NLCD data was upscaled accordingly.
 162 Each NLCD grid element, or pixel, is constituted of an array of values ranging from 0 to 1, with each value
 163 corresponding to the fraction of pixel that is determined by each land cover class.

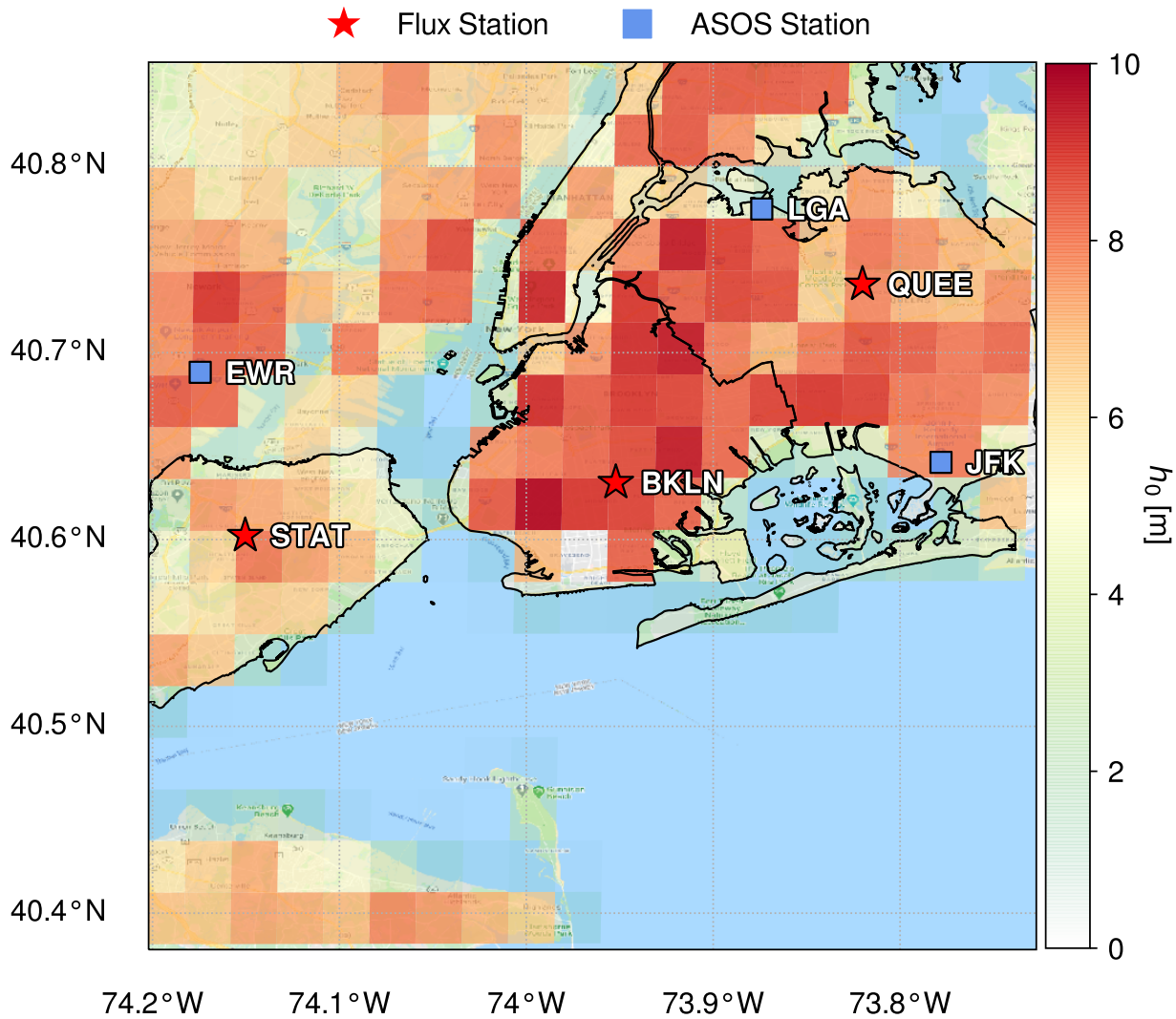


Figure 3: Gridded map of roughness heights across the New York City metropolitan area. Note flux and observation station denoted by their corresponding symbols.

164 Roughness heights used for the WRF model are likewise used for this model for the corresponding NLCD
 165 classes. Specific h_0 values are used for urban areas, defined as “Developed, Low Intensity”, “Developed,
 166 Medium Intensity”, and “Developed, High Intensity” by the NLCD classification system. The corresponding
 167 WRF classes are “Low-Density Residential”, “High-Density Residential”, and “Commercial”, respectively.
 168 The roughness heights defined by the WRF for “Low-Density Residential”, “High-Density Residential”, and
 169 “Commercial” areas are 5, 7.5, and 10 m, respectively. These values were used in the weighted-averaging
 170 scheme to obtain approximate roughness heights for the model.

171 To estimate the roughness height corresponding to each 2 x 2 km pixel, an inner product was taken using
 172 the land cover class roughness heights and the land cover class percentages.

173 2.3 GOES-16 Land Surface Temperature Product

174 The latest Geostationary Operational Environmental Satellite (GOES), GOES-16, is operated by the Na-
175 tional Aeronautic and Space Administration (NASA) and the National Oceanic and Atmospheric Adminis-
176 tration (NOAA) located over the western Atlantic Ocean that focuses on observation of North and South
177 America.

178 A number of products derived from the satellite radiance data are offered by the satellite, including a Land
179 Surface Temperature (LST) product. It is available for public use at a moderate spatial resolution of 2 x 2 km
180 and a high temporal resolution of 5 minutes ([NOAA/NESDIS/STAR \(2016\)](#)). The LST is calculated using
181 GOES-16 infrared bands 14 and 15. This product features a desirable balance of spatiotemporal resolution
182 and high accuracy (<2.5 K) ([Valenti \(2017\)](#)), making it an invaluable input to the model. The LST product
183 is available in a gridded netCDF (.nc) format, with data corresponding to latitude and longitude mapped
184 over the spatial extent of satellite observations. The data is filtered based on image quality, which is largely
185 dependent on sky conditions (i.e. cloud cover). Therefore, dates within the study timeframe with clear skies
186 or few clouds (<25% sky cover, per METAR ([World Meteorological Organization 2008](#)) were selected to
187 ensure high-quality LST for input to the model. The data used for the model was limited to a 0.5 degree
188 extent encompassing the most heavily-urbanized portion of the New York City metropolitan area, extending
189 from approximately (40.8805 N, 74.2021 W) to (40.3805 N, 73.7021 W), spanning approximately 190 km².
190 On a 2 x 2 grid, this represents approximately 380 pixels over which data was obtained for the metropolitan
191 area.

192 Another major component of the model is an urban air temperature model that takes GOES-16 LST
193 product data as an input and uses a diurnal regressive algorithm to calculate air temperature at a height of
194 2 m AGL ([Hrisko et al. 2020](#)). The model has been shown to calculate air temperatures in areas featuring a
195 range of land cover classes with high accuracy, specifically in urban areas (RMSE of 2.6 K relative to ground
196 station observations). Inputs to the model are LST, elevation, NLCD land cover class, and coordinates. The
197 model output is a gridded dataset with temperature values. For reference, the data is produced on a 2 x 2
198 km grid to match the gridded data format of the GOES-16 LST product.

199 2.4 Ground Station Observation Data

200 Model inputs for air pressure (p) and wind speed (u_r) were obtained from various Automated Surface
201 Observing System (ASOS) stations in the New York City metropolitan area. The ASOS network, which is
202 operated by NOAA, features over 900 sites in the United States, allowing for weather conditions at many
203 locations within the continental United States to be adequately represented by ASOS data.

204 Each ASOS station collects a wealth of information regarding weather conditions most relevant for
205 aviation purposes, including air temperature, dew point temperature, air pressure, wind speed and direction,
206 and sky cover. Each station generally records data at a frequency of 5 minutes, providing reasonable spatial
207 and excellent temporal frequencies for model data input.

208 Four (4) stations are located within the spatial domain evaluated in this study (see Figure 3 for reference):
209 John F. Kennedy International Airport (JFK) (40.6413° N, 73.7781° W), LaGuardia Airport (LGA) (40.7769°
210 N, 73.8740° W), Newark Liberty International Airport (EWR) (40.6895° N, 74.1745° W), Central Park
211 (40.7790° N 73.9693° W).

212 The ASOS stations closest to each observation site are selected for data collection. Specifically, these
213 ASOS stations are JFK (corresponding to Brooklyn), LGA (Queens), and EWR (Staten Island).

214 The model was validated using the New York State (NYS) Mesonet observation network ([Mesonet 2020](#)).

215 The network features 17 flux stations throughout the state of New York, with 3 stations located within New
216 York City - one each in the boroughs of Brooklyn (BKLN) (40.631762° N, 73.953678° W), Queens (QUEE)
217 (40.734335° N, 73.815856° W), and Staten Island (STAT) (40.604014° N, 74.148499° W). The flux network
218 stations record parameters relevant to the surface energy budget, including net radiation R_N , upward surface
219 latent heat flux Q_L , and upward surface sensible heat flux Q_H .

220 Each flux station is equipped with a net radiometer (manufactured by Kipp Zonen CNR4), ground
221 heat flux plates (Hukseflux), and a closed-path eddy covariance system (CPEC200, Campbell Scientific, Inc)
222 consisting of a sonic anemometer and gas analyzer. The net radiometer and eddy covariance system are
223 installed at 8 m AGL, while the ground plates are installed at a depth of 6 cm below ground. Station flux
224 measurements are reported every 30 minutes. The eddy covariance system was used to measure Q_H for the
225 duration of the validation period.

226 These stations were chosen due to the high sampling frequency and their locations in areas of the city
227 with distinct surrounding land cover types, rendering them useful for validating a model intended to provide
228 output with fine spatial resolution. NYS Mesonet data used for validation spans a full calendar year, from
229 1 June 2019 to 31 May 2020. All stations were operational and recorded data during the extent of the
230 validation time period.

231 **2.5 Urbanized Weather Research and Forecasting (uWRF) Model**

232 The Weather Research and Forecasting (WRF version 3.9.9.1) model with an urbanization option is used in
233 this study to compare and validate the satellite-derived Q_H values.

234 The uWRF was initialized with the North American Mesoscale (NAM) forecast at 12-km resolution. The
235 uWRF was run on multi-domain mode centered over New York City with the following domain resolutions:
236 9 km (120x120 grid), 3 km (121x121), and 1 km (85x82) with 51 vertical levels; the first level was located
237 at a height of 10 m with 30 additional levels below 1000 m. The uWRF was run for 4 days, chosen to be
238 roughly characteristic of each season: October 2019 (autumn), 23 December 2019 (winter), 20 January 2020
239 (winter), 12 May 2020 (spring).

240 The model was run with the Dudhia scheme (Dudhia (1989)) for shortwave radiation and the Rapid
241 Radiative Transfer Model for longwave radiation (Mlawer et al. (1997)). For the planetary boundary layer
242 (PBL) parameterization, the Mellor-Yamada-Janjic scheme (Janjić (1994)) was used while the land surface
243 fluxes for non-urban cover were parameterized using the NOAH scheme (Niu et al. (2011)). Cumulus param-
244 eterization was used for the coarser outer grid domains. For urban fluxes, the coupled Building Environment
245 Parameterization and Building Energy Model (BEP-BEM) was used (Salamanca & Martilli (2010)). Land
246 cover in New York City was represented by the Primary Land Use Tax Lot Output (PLUTO) database.
247 Similar configurations have been used in numerous previous studies (Gutiérrez et al. (2015), Gamarro et al.
248 (2019), Hrisko et al. (2021)).

249 **3 Results**

250 **3.1 Model Performance against Ground Stations**

251 The study period for the model spanned from 1 June 2019 (Julian day 152) to 31 May 2020 (Julian day 152).
252 Approximately 44 days over the course of the study period were selected for model validation. The selection
253 criteria included sky cover classified as “CLR” (clear sky) or “FEW” (few clouds) at each ASOS observation
254 station continuously over a 24-hour period and operational flux network status. For validation purposes,

model runs were initially performed at the latitude and longitude corresponding to each flux station. The corresponding GOES-16 grid location, or pixel, was used for the LST and T_{air} . The closest ASOS station was used to provide inputs of p and u (the distance between the study location and the corresponding ASOS station is a potential source of error that is discussed further). In total, 3 pixels were analyzed for validation purposes at hourly intervals over the selected days, resulting in a total of approximately 3,200 data points.

Four (4) statistical measures were used to determine model performance relative to ground stations: root-mean-square error (RMSE), mean bias error (MBE), the Nash-Sutcliffe model coefficient (NSC), and the coefficient of determination (R^2). Each measure is defined as follows:

$$RMSE = \sqrt{\frac{1}{N} \sum_{i=1}^N (Q_{H,i,m} - Q_{H,i,o})^2} \quad (10)$$

$$MBE = \frac{1}{N} \sum_{i=1}^N (Q_{H,i,m} - Q_{H,i,o}) \quad (11)$$

$$NSC = 1 - \frac{\sum_{i=1}^N (Q_{H,i,m} - Q_{H,i,o})^2}{\sum_{i=1}^N N(Q_{H,i,o} - \overline{Q}_{H,o})^2} \quad (12)$$

$$R^2 = 1 - \frac{\sum_{i=1}^N (Q_{H,i,m} - \overline{Q}_{H,i,o})^2}{\sum_{i=1}^N N(Q_{H,i,o} - \overline{Q}_{H,o})^2} \quad (13)$$

The statistical results of the study period, as defined in Equations X-Y above, are shown in Table 1.

Table 1: Model performance statistics against ground station data over the study period (2019 June - 2020 May). RMSE and MBE have units of Wm^{-2} .

Station	Points	RMSE	MBE	NSC	R^2
BKLN	1153	58.96	27.96	0.27	0.71
QUEE	1173	43.61	16.01	0.62	0.75
STAT	1263	38.00	4.17	0.67	0.73

3.1.1 Overall Results

Over the timeframe studied, the model featured a RMSE of $44.6 Wm^{-2}$, a bias of $12.4 Wm^{-2}$, an NSC value of 0.59, and a R^2 value of 0.71. The performance statistics suggest the model displayed reasonable agreement with the ground observations and performed satisfactorily, per the definition provided for the Nash-Sutcliffe coefficient by [Moriasi et al. \(2007\)](#). Model performance as a function of spatial and temporal variability will be discussed in this section. Temporal variability will be discussed on two distinct timescales, seasonal and daily, to improve understanding of model behavior and differences driven by changes in time on large and small temporal scales.

Nonetheless, the model showed considerable error from the ground observation data, and potential causes will be addressed further in the paper.

3.1.2 Geospatial Variability

The spatial distribution of Q_H was of interest in this study due to the heterogeneity of the land cover types present within the metropolitan area. The spatial distribution of Q_H at different times during a day in late October 2019 is shown in Figure 5. The Q_H at 14:00 UTC (10:00 local time) is shown to be positive at almost every pixel with relatively low magnitudes ($<100 W\cdot m^{-2}$), which is within the expected range of values for the mid-morning. At 17:00 UTC (13:00 local time), Q_H is near its peak value in most neighborhoods, with values nearing $300 W\cdot m^{-2}$ in sections of Queens and Newark. Decreasing values towards the northwestern outer edges (upper-left of the plot) of the metropolitan area correspond to areas with significant vegetative

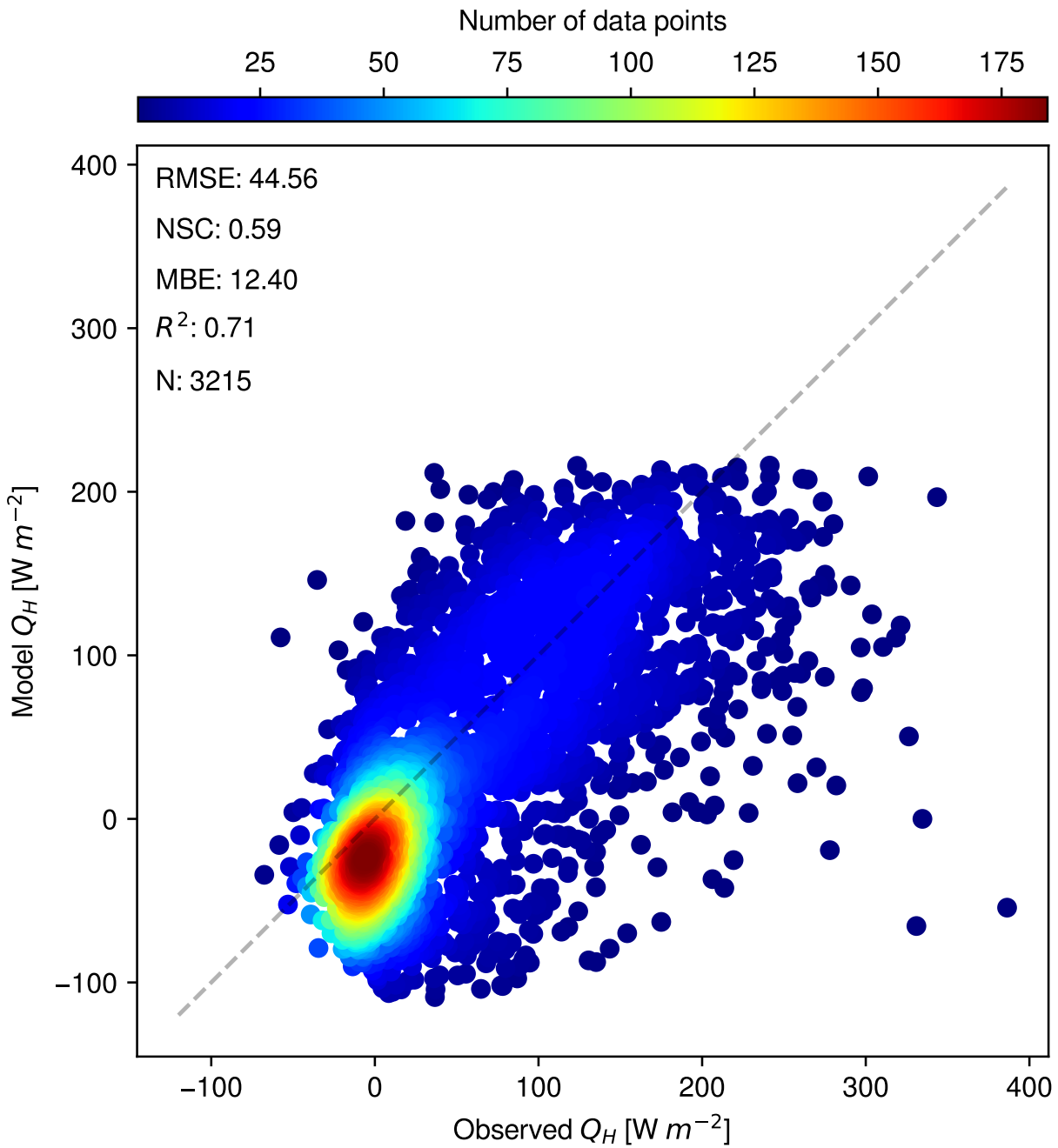


Figure 4: Comparison of model and observed Q_H from 1 June 2019 to 31 May 2020.

285 cover in suburban areas. At 20:00 UTC (16:00 local time), Q_H is seen to be decreasing from its peak value,
 286 which is a result of the surface layer air temperature increasing and approaching the land surface temperature.
 287 At 23:00 UTC (19:00 local time), Q_H nears zero as the sun sets and the land surface temperature decreases.
 288 Note that areas on the outer edges of the metropolitan area begin to display negative values of Q_H (equivalent
 289 to positive downward surface sensible heat flux) while more highly-urbanized areas continue to demonstrate
 290 positive Q_H . This correlates with the elevated heat storage (Q_S) that has been found to last longer into the
 291 nighttime hours in urban areas as compared to rural areas (Grimmond & Oke (1999a), Hrisko et al. (2021)).
 292 Based on the results presented in Table 1, it is apparent that Staten Island (STAT) features better model
 293 correlation than Brooklyn (BKLN) or Queens (QUEE) over all metrics except R^2 , although it is similar in
 294 value to the other 2 stations. The Staten Island flux tower is located in a less urbanized vicinity than the
 295 others (57.4% developed, per NLCD classifications) compared to Brooklyn (99.7% developed) and Queens
 296 (82.1% developed). This disparity in urbanization may indicate that land cover properties may be more
 297 homogeneous and extraneous heating sources (i.e. building processes, exhaust from utilities) may play less
 298 of a role in near-surface heating than in more heavily-urbanized areas. However, to properly determine any
 299 correlation between land cover type and model performance, validation is needed against additional flux
 300 towers over a wider range of land cover types within the city to increase confidence in any observed trends.

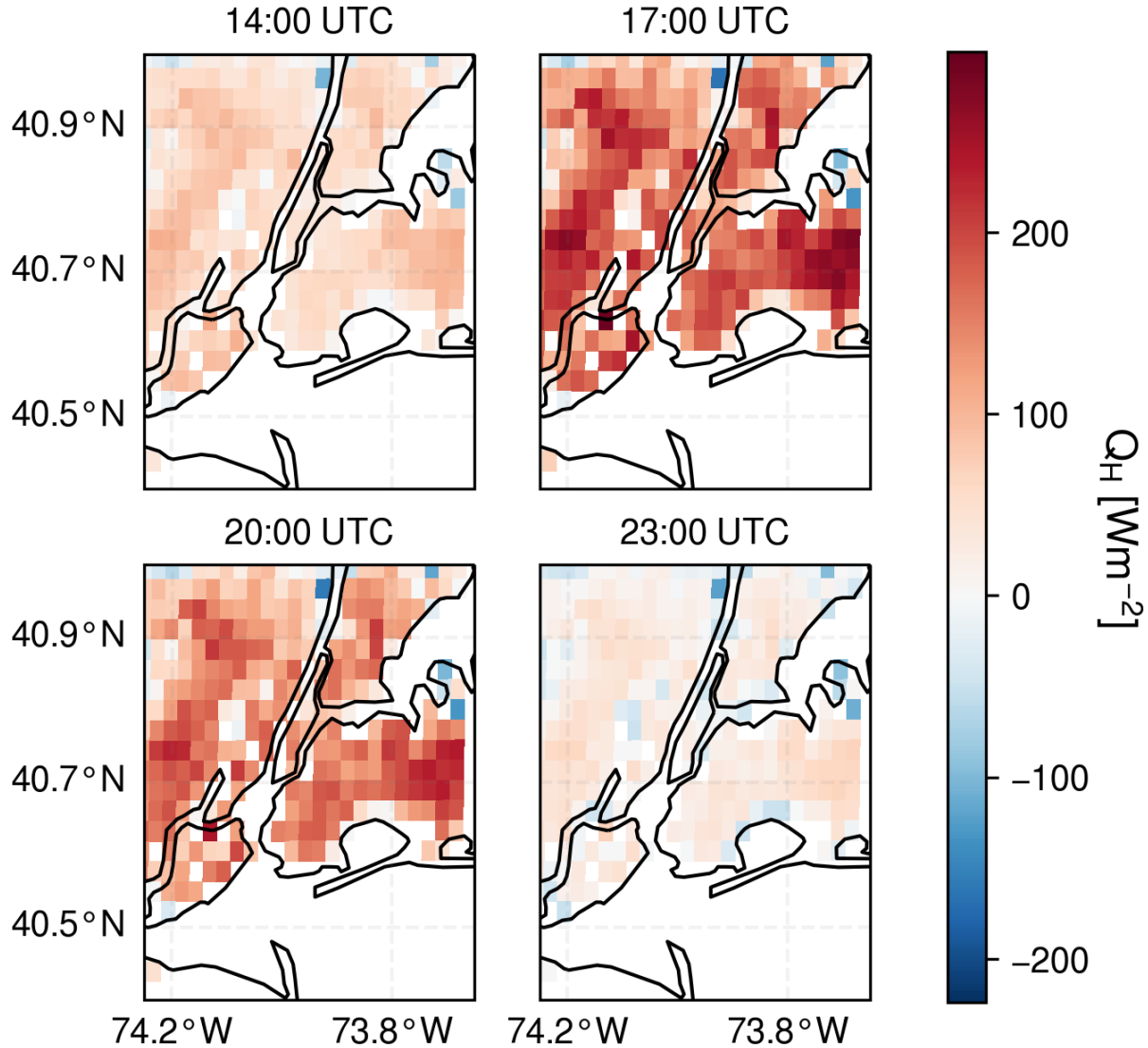


Figure 5: Q_H (W m^{-2}) in New York City on 24 October 2019 shown at 4 different times during the daytime. Note that on this date, New York City is UTC-4.

3.1.3 Seasonal Variability

The model exhibited variability in performance relative to the season during which runs were performed. As shown in Figure 6, the model appears to perform better in warmer months [summer (JJA) and spring (MAM)] than in cooler months. This is evident in the R^2 values of each season (0.80 and 0.79 for JJA and MAM, respectively) as compared to cooler months [autumn (SON) and winter (DJF)], which feature lower R^2 values (0.72 and 0.56, respectively). Model overprediction was more often visible for the winter months (DJF), while model imprecision, or spread, was most evident in both the autumn and winter months.

3.1.4 Daily Variability

Performance of the model against observed data over distinct portions of the day is displayed in Figure 7. The model performed fairly well during the daytime (10:00 - 20:00 UTC), with good agreement between the model and the observations ($\text{RMSE} = 46.2 \text{ W m}^{-2}$, $\text{MBE} = 1.35 \text{ W m}^{-2}$, $R^2 = 0.62$) across all stations. However, the model did not perform as well in the early nighttime hours due to an increased bias error (20:00 - 04:00 UTC) ($\text{RMSE} = 56.4 \text{ W m}^{-2}$, $\text{MBE} = 34.7 \text{ W m}^{-2}$, $R^2 = 0.67$) across all stations) and poorly during the pre-dawn hours due to a lack of correlation between modeled and observed data (04:00 - 10:00 UTC) ($\text{RMSE} = 46.2 \text{ W m}^{-2}$, $\text{MBE} = 24.4 \text{ W m}^{-2}$, $R^2 = -0.30$). For reference, New York City is UTC-4 during Eastern Daylight Time (EDT) (applies to months JJA, SON, and MAM) and UTC-5 during Eastern Standard Time (EST) (applies to months DJF). The performance error during the pre-dawn hours is likely due to the relationship between storage heat and sensible heat (Grimmond & Oke (1999a)) and will be

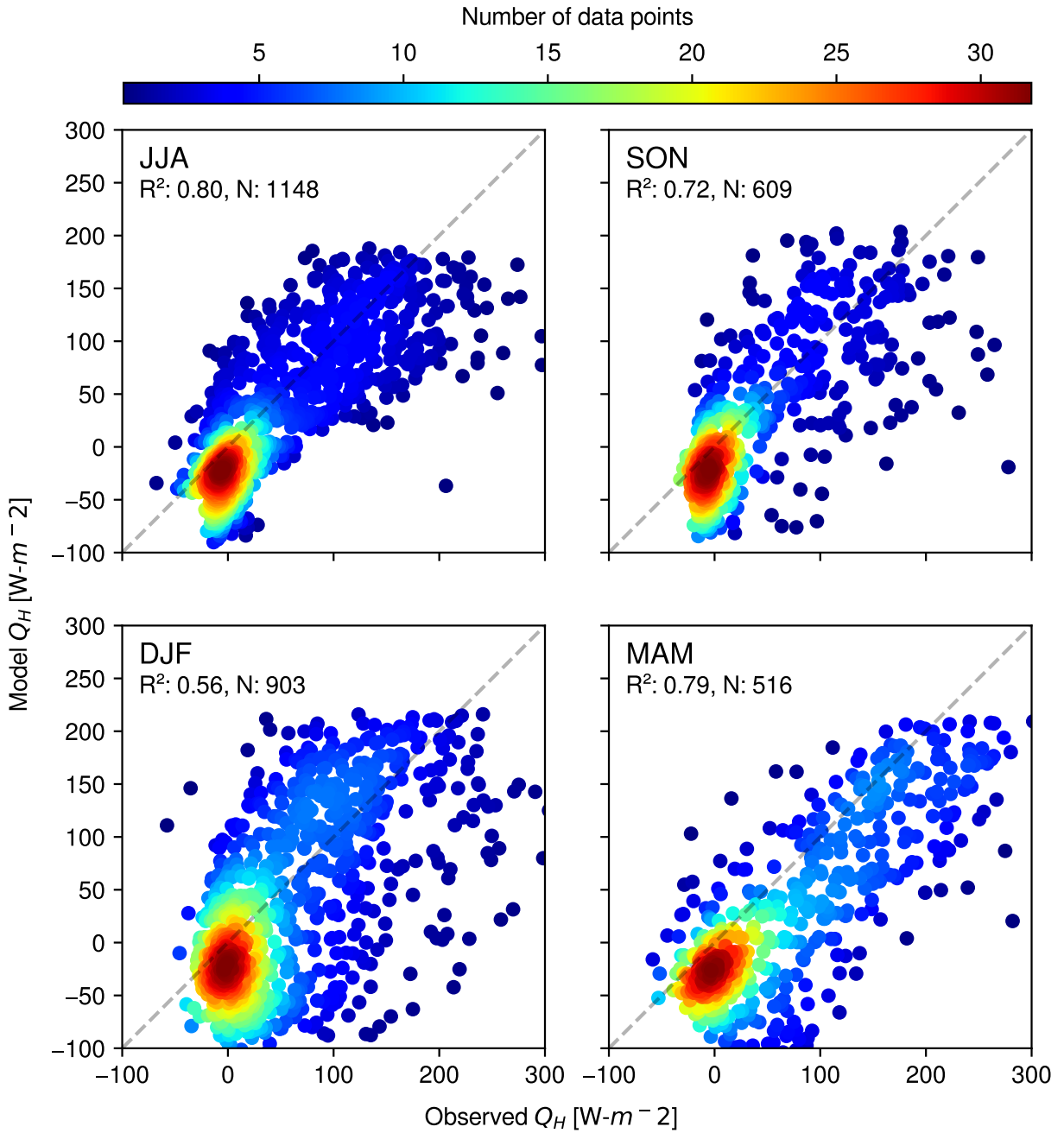


Figure 6: Comparison of model and observed Q_H divided into seasons. Note that the acronyms correspond to months in each season (for example, 'JJA' corresponds to June, July and August).

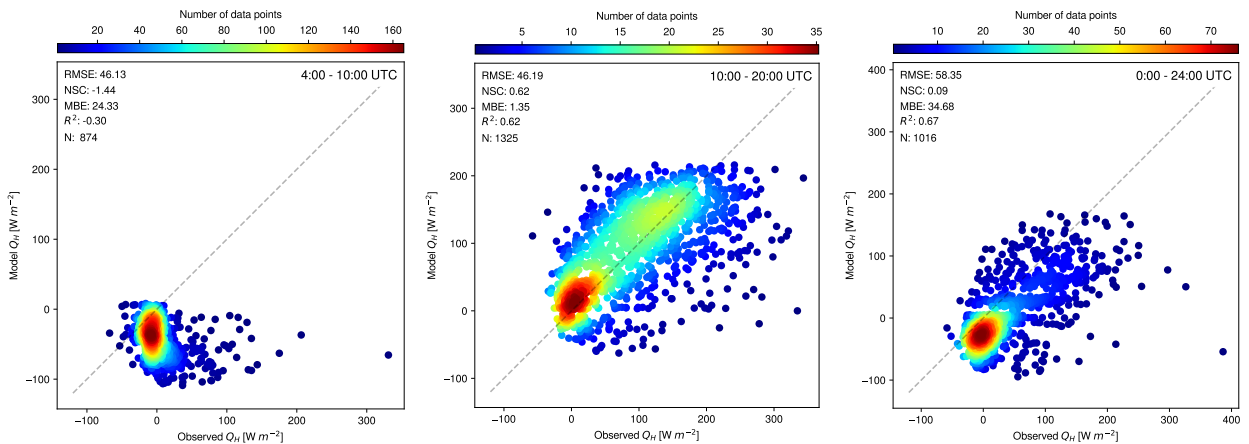


Figure 7: Comparison of model and observed Q_H divided into distinct periods of the day. (from left to right) early morning (pre-sunrise), daytime, evening and late night (post-sunset).

discussed further on in the paper.

As shown in Figure 8, these diurnal performance trends are further supported by timeseries data over 12 selected days in 4 different seasons in Queens (QUEE). The model performs considerably well during daytime hours, especially in the summer (JJA) and autumn (SON) months. However, the model consistently underestimates Q_H during nighttime hours - especially so in the winter (DJF) months.

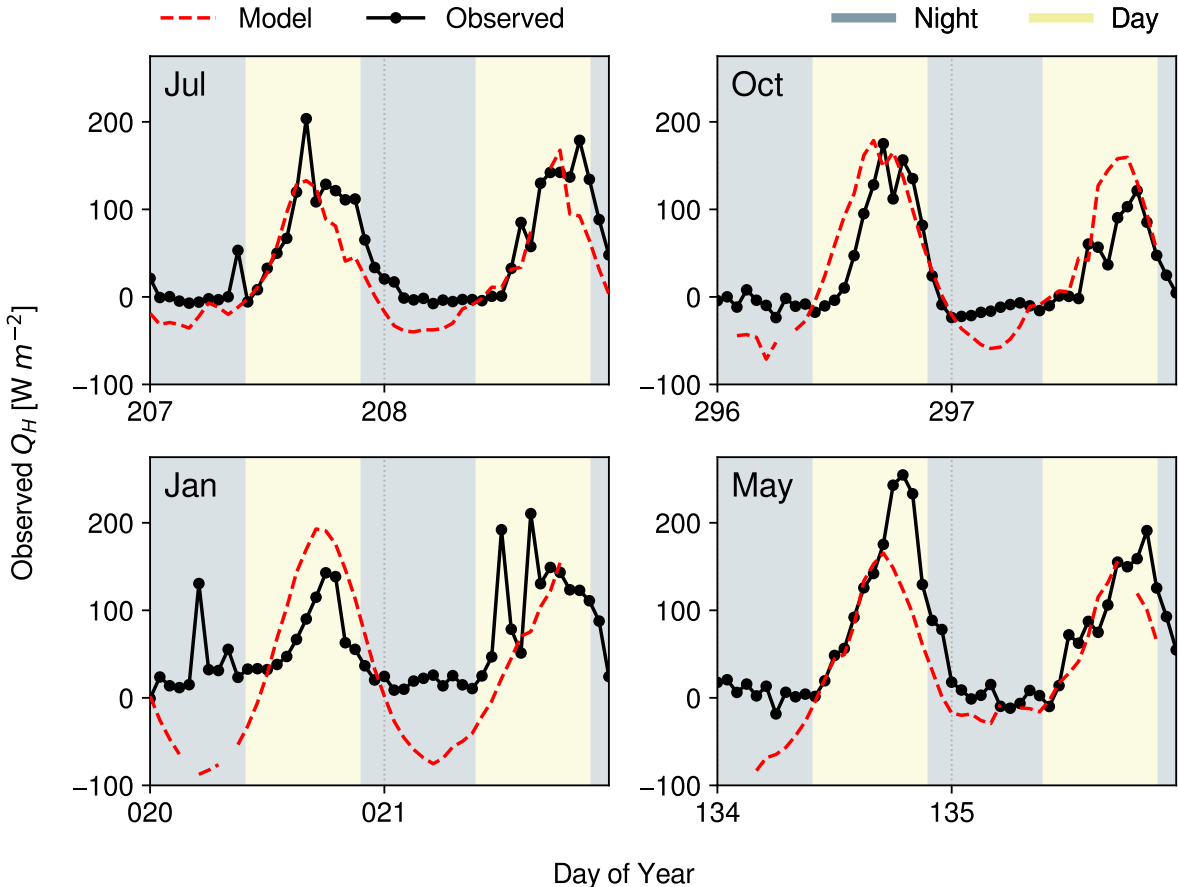


Figure 8: Timeseries comparison of model and observed Q_H for the Queens (QUEE) station for each season. Note that the acronyms correspond to months in each season (e.g. 'JJA' corresponds to June, July and August).

324 3.2 Model Performance against WRF

325 The uWRF model was used as a benchmark for model performance against ground station observations. The
 326 model was run on 4 separate days, for 24 hours each: 24 October 2019 (SON), 23 December 2019 (DJF-1), 20
 327 January 2020 (DJF-2), and 12 May 2020 (MAM). The spatial pixel nearest to each ground station was used
 328 for comparison. Each ground station used in the Q_H to ground station validation study (BKLN, QUEE,
 329 STAT) was selected to produce the comparison.

330 Over the days analyzed in the study, the RMSE between the uWRF model and ground observation sta-
 331 tions was 108.1 W m^{-2} , with a MBE of -30.1 W m^{-2} , a NSC was -1.47 , and a R^2 of 0.63 . The performance
 332 statistics show considerably poorer performance than the dedicated Q_H model, relative to the ground sta-
 333 tions. The uWRF model consistently overpredicted daytime Q_H (see Figures 9 and 10), although it predicted
 334 nocturnal Q_H more accurately than the dedicated Q_H model.

335 4 Discussion

336 4.1 Diurnal Model Performance

337 The model performs much better during the daytime than during the nighttime. The difference in perfor-
 338 mance could be related to the prevailing atmospheric conditions; daytime transport of heat is facilitated
 339 by thermals (buoyancy generated turbulence) that are highly efficient in mixing heat and other scalars. In
 340 urban areas, the largest thermals could be of the size of the boundary layer, on the order of 1-2 km, which
 341 is close to the spatial resolution of GOES-16 pixels. In stark contrast, during the nighttime hours, when the
 342 urban atmosphere is less convectively active, the transport is mainly dominated by mechanical turbulence

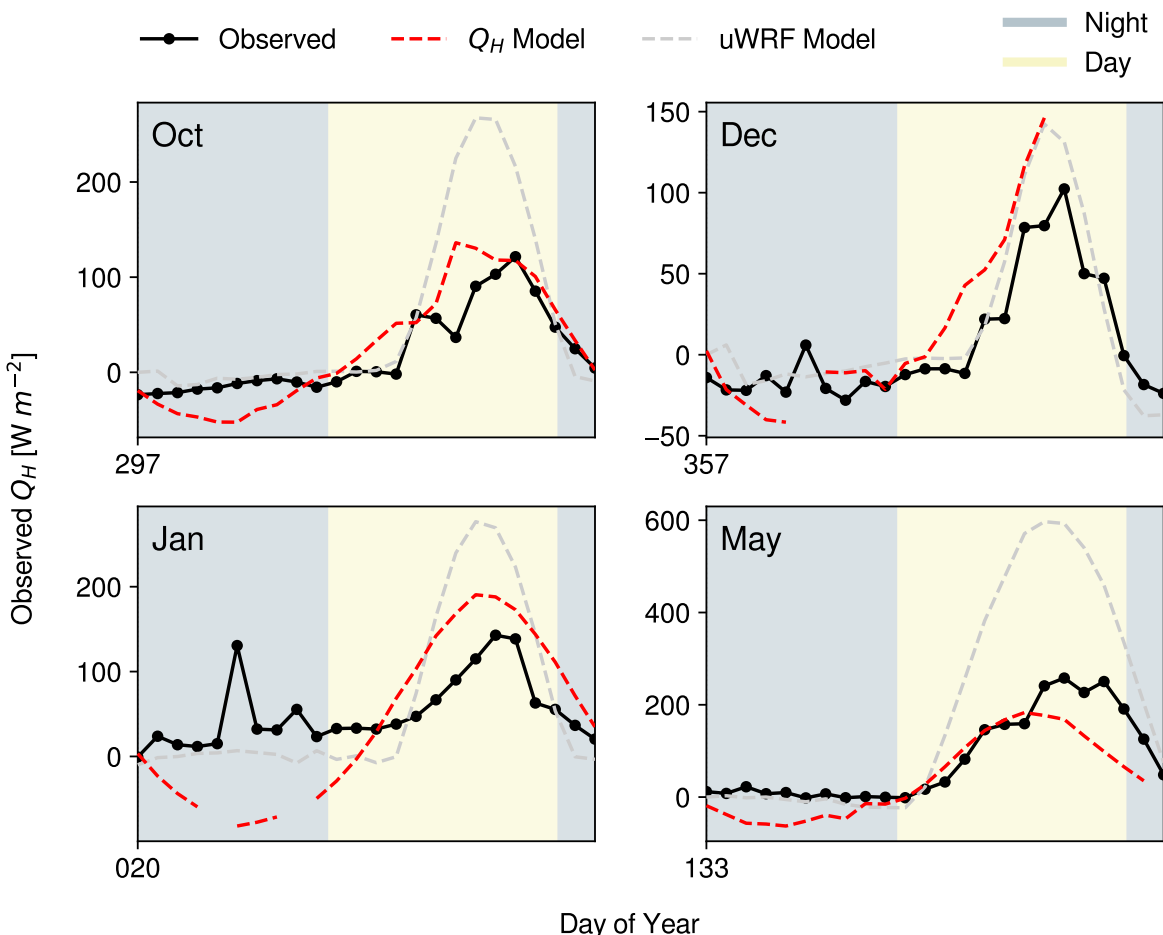


Figure 9: Observed and modeled (uWRF and dedicated) Q_H at days selected for uWRF study. Note that 'DJF-1' represents the date December 23, 2019 and 'DJF-2' represents January 20, 2020.

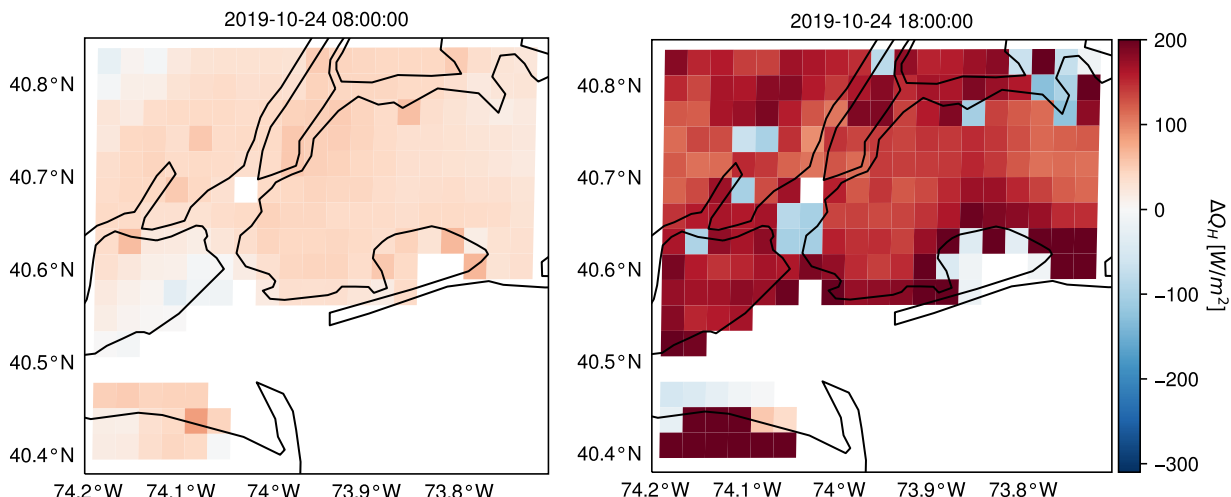


Figure 10: Gridded maps showing error between dedicated Q_H and uWRF models, October 24, 2019 at 08:00 (left) and 18:00 UTC (right). Light blue pixels correspond to areas with mostly covered in water/marsh.

343 through wind shear, which is highly localized. Additionally, the wind field used in the model to derive u^*
 344 is obtained from an ASOS station that might be unrepresentative of the nearest GOES-16 LST pixel. This
 345 error source is discussed further in the next section.

346 4.2 Potential Sources of Error

347 Numerous assumptions were made in the development of the model that may have contributed to model
 348 error.

349 A likely source of model error stemmed from the moderate spatial resolution of the GOES-16 LST product.
 350 The LST product features pixels at a spatial resolution of 2 km, which translates to 196 pixels spanning the

351 New York City area (approximate land area of 778 km^2). Although this allows for fragmentation of the city
352 into pixels that can distinguish districts (such as boroughs for New York City) from each other, the lack of
353 higher resolution may fail to capture localized phenomena from smaller neighborhoods in each district, such
354 as the effects of urban street canyons ([Xiaomin et al. \(2006\)](#), [Erell & Williamson \(2006\)](#)). This is important
355 due to the highly variable land cover types that exist between neighborhoods in large cities such as New
356 York City ([Hamstead et al. \(2016\)](#)).

357 Another potential source of error comes from the selection of h_0 for land cover types classified as "urban"
358 (Developed, High Intensity; Developed, Medium Intensity; Developed, Low Intensity; per the NLCD). The
359 assumed values were derived from the WRF-ARW model assumptions. However, the values may vary widely
360 from city to city, depending on the average heights of buildings in each. In a city with a large number of
361 tall buildings ($>10 \text{ m}$) such as New York City, larger values of h_0 for each class may be more suitable to
362 properly parameterize the boundary layer wind profile.

363 Another additional source of error between the model and the NYS Mesonet observations is the distance
364 between the ASOS stations, where wind speed data is collected, and the Mesonet flux stations, where flux
365 data is collected. The ASOS stations used for data collection are all located at large airports that feature
366 large expanses of flat surfaces surrounding the station instrumentation with minimal upwind obstructions.
367 By comparison, each flux station is located in a moderately- to heavily-urbanized area, reducing the upwind
368 fetch and exposing instrumentation to hyperlocal turbulence is a direct function of the surrounding geom-
369 etry [Kastner-Klein et al. \(2004\)](#). Additionally, the highly heterogeneous land cover in the New York City
370 metropolitan area can create highly-localized wind fields due to phenomena such as the urban street canyon
371 effect [Park et al. \(2012\)](#).

372 4.2.1 Environmental conditions of flux measurement sites

373 A source of potential error with the validation procedure is the "representativeness" of the observation
374 sites of their surroundings (how well the atmospheric conditions at the site match those of their respective
375 vicinities).

376 The World Meteorological Organization (WMO) defines a classification system for land surface observa-
377 tion stations to determine how representative the observation site is of its surroundings ([World Meteorological
378 Organization \(2010\)](#)). The basis for the representativeness of the sites depends on numerous factors, includ-
379 ing local obstacles, artificial heating sources, and so on. The classifications are on a 5-point scale, where 1
380 represents an ideal reference site for a wide area and 5 represents an inappropriate reference site for a wide
381 area.

382 The classifications for each Mesonet observation site are given in Table 2. The classifications are catego-
383 rized based on parameters relevant to determining atmospheric conditions.

Table 2: WMO classifications for NYS Mesonet flux network stations in New York City.

Site	Temperature & Humidity	Surface Wind	Precipitation	Direct Radiation	Global and Diffuse Radiation
BKLN	5	3	2	1	1
QUEE	5	3	4	2	1
STAT	5	3	2	2	1

384 Per Table 2, "Temperature/Humidity" and "Surface Wind" are both categories in which the urban sites
385 fare poorly. Although this does not render the data as inaccurate, a degree of uncertainty is introduced to the
386 validation data, which may increase errors for model parameters such as air temperature (T_{air}) and friction
387 velocity (u^*). Moreover, the poor classification indicates that site measurements may only be appropriate

388 for highly-localized areas surrounding the site, per the WMO definition of the classification system. This
389 may explain differences in observation data between the flux station and ASOS data, which can introduce
390 additional error into the study.

391 An additional phenomenon observed during model review is latency in data collection at the observation
392 station. On occasion, the model predicted a daytime spike in Q_H prior to the observation station on the
393 order of an hour, which contributes to error in the statistical analysis of the datasets.

394 4.3 Literature Review and Comparison

395 A challenge in comparing model performance with results present in the reviewed literature is the lack
396 of research performed with a similar methodology in urban areas. A list of comparable studies has been
397 compiled and evaluated, organized into satellite-based, airborne, and ground-based observations for Q_H in
398 urban and rural areas.

399 Few studies in the reviewed literature have modeled urban Q_H using satellite-based remote sensing data
400 ([Rigo & Parlow \(2007\)](#), [Liu et al. \(2012\)](#)). A study by [Rigo & Parlow \(2007\)](#) of model estimation of surface
401 heat fluxes using several satellite platform images was performed for Basel, Switzerland. The study used
402 satellite imagery as inputs to several models, including the Objective Hysteresis Model (OHM) to model
403 heat storage ([Oke & Cleugh \(1987\)](#), [Grimmond & Oke \(1999b\)](#)), to analyze model performance against
404 time-averaged heat flux data, with very good agreement ($R^2 = 0.95$ using the OHM approach). However,
405 image frequency from the satellite data used was very low compared to that of GOES-16 satellite imagery.
406 Additionally, only 2 days during the summer were used for data collection, rendering any comparisons of
407 annual performance variability impossible. In [Liu et al. \(2012\)](#), ASTER satellite data was used as input to
408 a model to estimate surface fluxes over a 25 km^2 area, encompassing a variety of land cover types that
409 range from highly-developed urban areas to open green space to crop fields. The study results yielded some
410 correlation with related atmospheric parameters for similar settings in the literature, but no observation
411 data was used to further validate findings from the study. Additionally, the study was performed for a single
412 point in time, preventing any temporal variability analysis from being performed.

413 Several studies have been performed to determine the ability to estimate Q_H from airborne observations
414 ([Xu et al. \(2008\)](#), [Kim & Kwon \(2019\)](#)). A study by [Xu et al. \(2008\)](#) showed that remote sensing is a viable
415 way to determine the variation of Q_H in urban areas by using an airborne spectrometer to analyze a section
416 of Shanghai to determine land cover information, surface temperature, and other parameters relevant to the
417 calculation of Q_H . However, this study used a helicopter-mounted sensor to image a relatively small area (2
418 km square) for a single day. Although this method was able to image urban areas at ultrahigh resolutions
419 of 30 m, the lack of spatiotemporal variability and the expenses associated with the study prevent it from
420 being a practical method for estimating Q_H for larger areas over extended periods of time. In [Kim & Kwon](#)
421 ([2019](#)), Q_H and other related atmospheric parameters were measured using an unmanned aerial vehicle
422 (UAV) over various non-urban land cover types and found strong correlation between UAV estimations and
423 ground-measured data. However, these trials were performed over relatively homogeneous and undeveloped
424 land cover surfaces, so direct comparison is not appropriate.

425 Ground-based observations are a common research theme with a similar goal of using cost-effective
426 methods to determine Q_H . Another study ([Nadeau et al. \(2009\)](#)) found reasonable agreement ($R^2 = 0.61$)
427 between a singular profile measurements and a network of ground observation stations on a university campus
428 with highly-heterogeneous land cover in Lausanne, France. The study also reinforced the importance of a
429 spatially-dense observation network in urban areas to provide high-resolution meteorological measurements.

430 However, the study was limited to an area far smaller (750 x 500 m) than a city, preventing any study on
431 spatial variability in results within cities.

432 4.4 Application Potential

433 The dedicated Q_H model leverages open-access satellite and land cover data that allows for a cost-effective
434 way to analyze sensible heat flux in urban areas. The model enables Q_H to be estimated at any point within
435 the scope of the GOES-16 satellite imagery with reasonable accuracy, removing constraints to single-point
436 observation stations.

437 Consequently, the model can be used to identify a number of factors that contribute to or correlate with
438 the effects of urban heat islands in major cities, which directly relate to the vulnerability of a neighborhood
439 due to the effects of climate. The model is especially valuable in locations that are not in close proximity to
440 flux observation stations.

441 Additionally, the model can be used as a module for high-resolution numerical weather models to improve
442 the spatial resolution of Q_H estimation in areas of interest. Moreover, the geographical extent spanned by
443 the GOES-16 satellite imagery allows the model to be used over wide swaths of the CONUS, allowing for
444 Q_H estimations to be performed efficiently over large areas at hourly intervals.

445 4.5 Future Work

446 A number of factors from this study motivate future work to improve the accuracy of the model.

447 A possible improvement to the model involves validation at a range of test sites with similar land cover
448 heterogeneity at different locations. Due to the study focusing on one city, atmospheric conditions that are
449 a function of location, such as air pressure or advective fluxes, may not be fully accounted for in this model,
450 potentially requiring a modification of assumptions or parameter values.

451 Another improvement to the model involves downscaling of the z_m grid. A critical component of the
452 model is the calculation of z_m , which is a factor in nearly every component of the turbulence parameterization.
453 Due to the highly heterogeneous nature of urban areas, z_m must be calculated at an extremely high spatial
454 resolution to properly represent the corresponding land cover. Although the NLCD has a spatial resolution of
455 30 meters, the spatial resolution of the z_m calculations is driven by the GOES-16 satellite spatial resolution.
456 Therefore, a higher-resolution satellite or a downscaling algorithm for the GOES-16 LST product would
457 likely improve the calculation of z_m and in turn, the calculation of all dependent parameters.

458 The estimation of nocturnal sensible heat flux is another critical component to improving model accuracy.
459 The model often underperforms relative to the observation sites despite good approximation during the day.
460 The connection between sensible and storage heat is a likely explanation for the near-zero and positive
461 upward surface sensible heat flux at night ([Grimmond & Oke \(1999a\)](#)). Incorporation of this connection into
462 the turbulence parameterization may improve model accuracy, and this topic requires further exploration.

463 5 Conclusions

464 A dedicated satellite-based model using NOAA's GOES-16 data to calculate sensible heat flux in urban areas
465 was introduced. The model couples GOES-16' LST and publicly-accessible land cover data in an iterative
466 turbulence parameterization based on MOST to provide a product that is capable of calculating Q_H in areas
467 with highly heterogeneous land cover. The performance of the model was validated using an ample set of
468 ground station observations in New York City. Additionally, the model was compared to an urbanized WRF

469 model and performed significantly better relative to observational data. Accordingly, these validation and
470 comparison procedures suggest that the dedicated model is reasonably accurate in estimating Q_H in urban
471 areas at sub-hourly timescales.

472 Over the duration of the validation period, the RMSE between the model and observational data was
473 44.6 W m^{-2} , with a MBE of 12.4 W m^{-2} , a model NSC of 0.59, and a R^2 coefficient of 0.71. This presents a
474 significant improvement over the numerical WRF model run over fewer days in the same validation period
475 (RMSE of 108.1 W m^{-2} , MBE of -30.1 W m^{-2} , NSC of -1.47 and R^2 of 0.63). The model performed especially
476 well in warmer months (R^2 coefficients of 0.80 and 0.79 for summer and autumn, respectively) and during
477 the daytime and evening hours.

478 The development of a satellite-based Q_H model demonstrates the potential of the use of satellite data for
479 estimating atmospheric processes over large spatial and temporal domains. The ability to leverage this data
480 for usage in urban areas is valuable as this method resolves several limitations that are encountered in esti-
481 mating atmospheric processes in areas with highly heterogeneous land cover and an insufficient observational
482 infrastructure. This ability is especially important considering the impact of heat-related weather events on
483 human populations, allowing for risk assessment and mitigation strategies to become better informed with
484 improved supporting data.

485 6 Acknowledgments

486 This study is supported and monitored by The National Oceanic and Atmospheric Administration – Cooper-
487 ative Science Center for Earth System Sciences and Remote Sensing Technologies (NOAA-CESSRST) under
488 the Cooperative Agreement Grant NA16SEC4810008. The authors would like to thank The City College of
489 New York, NOAA-CESSRST program and NOAA Office of Education, Educational Partnership Program
490 for fellowship support for Gabriel Rios. The statements contained within the manuscript/research article
491 are not the opinions of the funding agency or the U.S. government, but reflect the author's opinions. The
492 research was also funded by the Department of Defense Army Research Office Grant No. W911NF2020126.

493 This research is made possible by the New York State (NYS) Mesonet. Original funding for the NYS Mesonet
494 was provided by Federal Emergency Management Agency grant FEMA-4085-DR-NY, with the continued
495 support of the NYS Division of Homeland Security Emergency Services; the state of New York; the Research
496 Foundation for the State University of New York (SUNY); the University at Albany, SUNY; the Atmospheric
497 Sciences Research Center (ASRC) at SUNY Albany; and the Department of Atmospheric and Environmental
498 Sciences (DAES) at SUNY Albany.

499 References

500 Best, M. (2005), 'Representing urban areas within operational numerical weather prediction models',
501 *Boundary-Layer Meteorology* **114**(1), 91–109.

502 Bureau, U. C. (2019), 'Population and Housing Unit Estimates Tables'.

503 **URL:** <https://www.census.gov/programs-surveys/popest/data/tables.html>

Businger, J. A., Wyngaard, J. C., Izumi, Y. & Bradley, E. F. (1971), 'Flux-profile relationships in the
atmospheric surface layer', *Journal of Atmospheric Sciences* **28**, 181 – 189.

503 **URL:** https://journals.ametsoc.org/view/journals/atsc/28/2/1520-0469_1971_028_0181_fprita20co2.xml

- 504 Chen, F., Kusaka, H., Bornstein, R., Ching, J., Grimmond, C., Grossman-Clarke, S., Loridan, T., Man-
 505 ning, K. W., Martilli, A., Miao, S. et al. (2011), ‘The integrated wrf/urban modelling system: develop-
 506 ment, evaluation, and applications to urban environmental problems’, *International Journal of Climatology*
 507 **31**(2), 273–288.
- 508 Chen, F. & Zhang, Y. (2009), ‘On the coupling strength between the land surface and the atmosphere: From
 509 viewpoint of surface exchange coefficients’, *Geophysical Research Letters* **36**(10).
- 510 **URL:** <https://agupubs.onlinelibrary.wiley.com/doi/abs/10.1029/2009GL037980>
- 511 Chrysoulakis, N., Grimmond, S., Feigenwinter, C., Lindberg, F., Gastellu-Etchegorry, J.-P., Marconcini,
 512 M., Mitraka, Z., Stagakis, S., Crawford, B., Olofson, F., Landier, L., Morrison, W. & Parlow, E. (2018),
 513 ‘Urban energy exchanges monitoring from space’, *Scientific Reports* **8**(1), 11498.
- 514 **URL:** <http://www.nature.com/articles/s41598-018-29873-x>
- 515 Dudhia, J. (1989), ‘Numerical study of convection observed during the winter monsoon experiment using a
 516 mesoscale two-dimensional model’, *Journal of Atmospheric Sciences* **46**(20), 3077–3107.
- 517 Dyer, A. J. (1974), ‘A review of flux-profile relationships’, *Boundary-Layer Meteorology* **7**(3), 363–372.
- 518 **URL:** <http://link.springer.com/10.1007/BF00240838>
- 519 Erell, E. & Williamson, T. (2006), ‘Simulating air temperature in an urban street canyon in all weather
 520 conditions using measured data at a reference meteorological station’, *International Journal of Climatology:
 521 A Journal of the Royal Meteorological Society* **26**(12), 1671–1694.
- 522 Feddema, J. J., Oleson, K. W., Bonan, G. B., Mearns, L. O., Buja, L. E., Meehl, G. A. & Washington, W. M.
 523 (2005), ‘The importance of land-cover change in simulating future climates’, *Science* **310**(5754), 1674–1678.
- 524 Gamarro, H., Gonzalez, J. E. & Ortiz, L. E. (2019), ‘On the assessment of a numerical weather prediction
 525 model for solar photovoltaic power forecasts in cities’, *Journal of Energy Resources Technology* **141**(6).
- Grimmond, C. S. B. & Cleugh, H. A. (1994), ‘A simple method to determine obukhov lengths for suburban
 areas’, *Journal of Applied Meteorology and Climatology* **33**(3), 435 – 440.
- URL:** https://journals.ametsoc.org/view/journals/apme/33/3/1520-04501994033_0435_asmtdo20co2.xml
- Grimmond, C. S. B. & Oke, T. R. (1999a), ‘Heat storage in urban areas: Local-scale observations and
 evaluation of a simple model’, *Journal of Applied Meteorology* **38**(7), 922 – 940.
- URL:** https://journals.ametsoc.org/view/journals/apme/38/7/1520-04501999038_0922_hsiual2.0.co2.xml
- Grimmond, C. S. B. & Oke, T. R. (1999b), ‘Heat storage in urban areas: Local-scale observations and
 evaluation of a simple model’, *Journal of Applied Meteorology* **38**(7), 922 – 940.
- URL:** https://journals.ametsoc.org/view/journals/apme/38/7/1520-04501999038_0922_hsiual2.0.co2.xml
- 526 Gutiérrez, E., González, J. E., Martilli, A., Bornstein, R. & Arend, M. (2015), ‘Simulations of a heat-wave
 527 event in new york city using a multilayer urban parameterization’, *Journal of Applied Meteorology and
 528 Climatology* **54**(2), 283–301.
- 529 Hamstead, Z. A., Kremer, P., Larondelle, N., McPhearson, T. & Haase, D. (2016), ‘Classification of the
 530 heterogeneous structure of urban landscapes (sturla) as an indicator of landscape function applied to
 531 surface temperature in new york city’, *Ecological Indicators* **70**, 574 – 585. Navigating Urban Complexity:
 532 Advancing Understanding of Urban Social – Ecological Systems for Transformation and Resilience.
- 533 **URL:** <http://www.sciencedirect.com/science/article/pii/S1470160X1500549X>

- 534 Hong, S.-Y. & Dudhia, J. (2012), 'Next-generation numerical weather prediction: Bridging parameterization,
535 explicit clouds, and large eddies', *Bulletin of the American Meteorological Society* **93**(1), ES6–ES9.
- 536 Hrisko, J., Ramamurthy, P., Melecio-Vazquez, D. & Gonzalez, J. E. (2021), 'Spatiotemporal variability of
537 heat storage in major u.s. cities—a satellite-based analysis', *Remote Sensing* **13**, 59.
538 **URL:** <https://www.mdpi.com/2072-4292/13/1/59>
- 539 Hrisko, J., Ramamurthy, P., Yu, Y., Yu, P. & Melecio-Vázquez, D. (2020), 'Urban air temperature model
540 using goes-16 lst and a diurnal regressive neural network algorithm', *Remote Sensing of Environment*
541 **237**, 111495.
542 **URL:** <http://www.sciencedirect.com/science/article/pii/S0034425719305140>
- 543 Imran, H. M., Kala, J., Ng, A. & Muthukumaran, S. (2018), 'Effectiveness of green and cool roofs in
544 mitigating urban heat island effects during a heatwave event in the city of melbourne in southeast australia',
545 *Journal of Cleaner Production* **197**, 393–405.
- 546 Janjić, Z. I. (1994), 'The step-mountain eta coordinate model: Further developments of the convection,
547 viscous sublayer, and turbulence closure schemes', *Monthly weather review* **122**(5), 927–945.
- 548 Kastner-Klein, P., Berkowicz, R. & Britter, R. (2004), 'The influence of street architecture on flow and
549 dispersion in street canyons', *Meteorology and Atmospheric Physics* **87**(1), 121–131.
- 550 Kato, S. & Yamaguchi, Y. (2005), 'Analysis of urban heat-island effect using aster and etm+ data: Separation
551 of anthropogenic heat discharge and natural heat radiation from sensible heat flux', *Remote Sensing of
552 Environment* **99**(1), 44 – 54. Scientific Results from ASTER.
553 **URL:** <http://www.sciencedirect.com/science/article/pii/S0034425705001707>
- 554 Kim, M.-S. & Kwon, B. H. (2019), 'Estimation of sensible heat flux and atmospheric boundary layer height
555 using an unmanned aerial vehicle', *Atmosphere* **10**, 363.
556 **URL:** <https://www.mdpi.com/2073-4433/10/7/363>
- 557 Launiainen, J. & Vihma, T. (1990), 'Derivation of turbulent surface fluxes — an iterative flux-profile method
558 allowing arbitrary observing heights', *Environmental Software* **5**(3), 113 – 124.
559 **URL:** <http://www.sciencedirect.com/science/article/pii/026698389090021W>
- 560 Leroyer, S., Bélair, S., Husain, S. Z. & Mailhot, J. (2014), 'Subkilometer numerical weather prediction in an
561 urban coastal area: A case study over the vancouver metropolitan area', *Journal of Applied Meteorology
562 and Climatology* **53**(6), 1433–1453.
- 563 Li, D. & Bou-Zeid, E. (2014), 'Quality and sensitivity of high-resolution numerical simulation of urban heat
564 islands', *Environmental Research Letters* **9**(5), 055001.
565 **URL:** <https://doi.org/10.1088/1748-9326/9/5/055001>
- 566 Liu, Y., Shintaro, G., Zhuang, D. & Kuang, W. (2012), 'Urban surface heat fluxes infrared remote sensing
567 inversion and their relationship with land use types', *Journal of Geographical Sciences* **22**(4), 699–715.
568 **URL:** <http://link.springer.com/10.1007/s11442-012-0957-7>
- 569 Mesonet, N. (2020), Flux network data resource, Technical report.
- 570 Mlawer, E. J., Taubman, S. J., Brown, P. D., Iacono, M. J. & Clough, S. A. (1997), 'Radiative transfer
571 for inhomogeneous atmospheres: Rrtm, a validated correlated-k model for the longwave', *Journal of
572 Geophysical Research: Atmospheres* **102**(D14), 16663–16682.

- 573 Monin, A. & Obukhov, A. (1954), 'Dimensionless characteristics of turbulence in the surface layer', *Akad.*
 574 *Nauk SSSR, Geofiz. Inst., Tr* **24**, 163–187.
- 575 Moriasi, D. N., Arnold, J. G., Liew, M. W. V., Bingner, R. L., Harmel, R. D. & Veith, T. L. (2007), 'Model
 576 evaluation guidelines for systematic quantification of accuracy in watershed simulations', *Transactions of*
 577 *the ASABE* **50**(3), 885–900.
- 578 Nadeau, D. F., Brutsaert, W., Parlange, M., Bou-Zeid, E., Barrenetxea, G., Couach, O., Boldi, M.-O.,
 579 Selker, J. S. & Vetterli, M. (2009), 'Estimation of urban sensible heat flux using a dense wireless network
 580 of observations', *Environmental fluid mechanics* **9**(6), 635–653.
- 581 Niu, G.-Y., Yang, Z.-L., Mitchell, K. E., Chen, F., Ek, M. B., Barlage, M., Kumar, A., Manning, K., Niyogi,
 582 D., Rosero, E. et al. (2011), 'The community noah land surface model with multiparameterization options
 583 (noah-mp): 1. model description and evaluation with local-scale measurements', *Journal of Geophysical*
 584 *Research: Atmospheres* **116**(D12).
- NOAA/NESDIS/STAR (2016), Geostationary operational environmental satellite (goes)-r series advanced
 baseline imager (abi) l2+ land surface temperature (lst) beta, provisional, and full validation readiness,
 implementation, and management plan (rimp), Technical report.
- URL:** https://goes-r.gov/products/RIMPs/RIMP_ABI-L2FSC_v1.0.pdf
- 585 Oke, T. R. & Cleugh, H. A. (1987), 'Urban heat storage derived as energy balance residuals', *Boundary-Layer*
 586 *Meteorology* **39**(3), 233–245.
- 587 **URL:** <http://link.springer.com/10.1007/BF00116120>
- 588 Park, S.-B., Baik, J.-J., Raasch, S. & Letzel, M. O. (2012), 'A large-eddy simulation study of thermal
 589 effects on turbulent flow and dispersion in and above a street canyon', *Journal of Applied Meteorology and*
 590 *Climatology* **51**(5), 829–841.
- 591 Pond, S., Fissel, D. B. & Paulson, C. A. (1974), 'A note on bulk aerodynamic coefficients for sensible heat
 592 and moisture fluxes', *Boundary-Layer Meteorology* **6**(1-2), 333–339.
- 593 **URL:** <http://link.springer.com/10.1007/BF00232493>
- Price, J. C. (1979), 'Assessment of the urban heat island effect through the use of satellite data', *Monthly*
Weather Review **107**(11), 1554 – 1557.
- URL:** https://journals.ametsoc.org/view/journals/mure/107/11/1520-049319791071554_aotuh120_c02.xml
- 594 Raupach, M. R. (1994), 'Simplified expressions for vegetation roughness length and zero-plane displacement
 595 as functions of canopy height and area index', *Boundary-Layer Meteorology* **71**, 211–216.
- 596 **URL:** <https://doi.org/10.1007/BF00709229>
- 597 Rigo, G. & Parlow, E. (2007), 'Modelling the ground heat flux of an urban area using remote sensing data',
 598 *Theoretical and Applied Climatology* **90**(3-4), 185–199.
- 599 Salamanca, F. & Martilli, A. (2010), 'A new building energy model coupled with an urban canopy pa-
 600 rameterization for urban climate simulations—part ii. validation with one dimension off-line simulations',
 601 *Theoretical and Applied Climatology* **99**(3), 345–356.
- 602 Schumacher, D. L., Keune, J., Van Heerwaarden, C. C., de Arellano, J. V.-G., Teuling, A. J. & Miralles,
 603 D. G. (2019), 'Amplification of mega-heatwaves through heat torrents fuelled by upwind drought', *Nature*
 604 *Geoscience* **12**(9), 712–717.

- 605 Skamarock, W., Klemp, J., Dudhia, J., Gill, D., Barker, D., Wang, W., Huang, X.-Y. & Duda, M. (2008),
 606 A Description of the Advanced Research WRF Version 3, Technical report, UCAR/NCAR.
- 607 **URL:** <http://opensky.ucar.edu/islandora/object/technotes:500>
- Stewart, J. B., Kustas, W. P., Humes, K. S., Nichols, W. D., Moran, M. S. & de Bruin, H. A. R. (1994),
 'Sensible heat flux-radiometric surface temperature relationship for eight semiarid areas', *Journal of Applied Meteorology and Climatology* **33**(9), 1110 – 1117.
- URL:** https://journals.ametsoc.org/view/journals/apme/33/9/1520-0450_1994_33_1110_shfrst20co2.xml
- 608 Valenti, J. (2017), Goes-r series product definition and users' guide, Technical report.
- 609 Vautard, R., Yiou, P., D'andrea, F., De Noblet, N., Viovy, N., Cassou, C., Polcher, J., Ciais, P., Kageyama,
 610 M. & Fan, Y. (2007), 'Summertime european heat and drought waves induced by wintertime mediterranean
 611 rainfall deficit', *Geophysical Research Letters* **34**(7).
- 612 Voogt, J. A. & Grimmond, C. S. B. (2000), 'Modeling surface sensible heat flux using surface radiative
 613 temperatures in a simple urban area', *Journal of Applied Meteorology* **39**(10), 1679 – 1699.
- 614 **URL:** https://journals.ametsoc.org/view/journals/apme/39/10/1520-0450_39_10_1679.xml
- 615 Voogt, J. & Oke, T. (2003), 'Thermal remote sensing of urban climates', *Remote Sensing of Environment*
 616 **86**(3), 370 – 384. Urban Remote Sensing.
- 617 **URL:** <http://www.sciencedirect.com/science/article/pii/S0034425703000798>
- 618 Wang, C., Myint, S. W., Wang, Z. & Song, J. (2016), 'Spatio-temporal modeling of the urban heat island in
 619 the phoenix metropolitan area: Land use change implications', *Remote Sensing* **8**(3), 185.
- 620 World Meteorological Organization, ed. (2008), *Aerodrome reports and forecasts: a users' handbook to the*
 621 *codes*, number no. 782 in 'WMO', 5th ed edn, WMO, Geneva, Switzerland. OCLC: ocn300459644.
- World Meteorological Organization, ed. (2010), *Measurements at Automatic Weather Stations*.
- URL:** https://library.wmo.int/docnum.php?explnum_id=3179
- 622 Xiaomin, X., Zhen, H. & Jiasong, W. (2006), 'The impact of urban street layout on local atmospheric
 623 environment', *Building and Environment* **41**(10), 1352–1363.
- 624 Xu, W., Wooster, M. & Grimmond, C. (2008), 'Modelling of urban sensible heat flux at multiple spatial
 625 scales: A demonstration using airborne hyperspectral imagery of shanghai and a temperature–emissivity
 626 separation approach', *Remote Sensing of Environment* **112**(9), 3493–3510.
- 627 Yang, L., Jin, S., Danielson, P., Homer, C., Gass, L., Bender, S. M., Case, A., Costello, C., Dewitz, J., Fry, J.,
 628 Funk, M., Granneman, B., Liknes, G. C., Rigge, M. & Xian, G. (2018), 'A new generation of the United
 629 States National Land Cover Database: Requirements, research priorities, design, and implementation
 630 strategies', *ISPRS Journal of Photogrammetry and Remote Sensing* **146**, 108–123.
- 631 **URL:** <https://linkinghub.elsevier.com/retrieve/pii/S092427161830251X>
- 632 Zhang, J., Draxl, C., Hopson, T., Delle Monache, L., Vanvyve, E. & Hodge, B.-M. (2015), 'Comparison of
 633 numerical weather prediction based deterministic and probabilistic wind resource assessment methods',
 634 *Applied Energy* **156**, 528–541.
- 635 Zilitinkevich, S. S. (1995), 'Air pollution theory and simulation', *Air Pollution* **3**, 53–60.

Figure 1

[Click here to access/download Figure fig1.pdf](#)

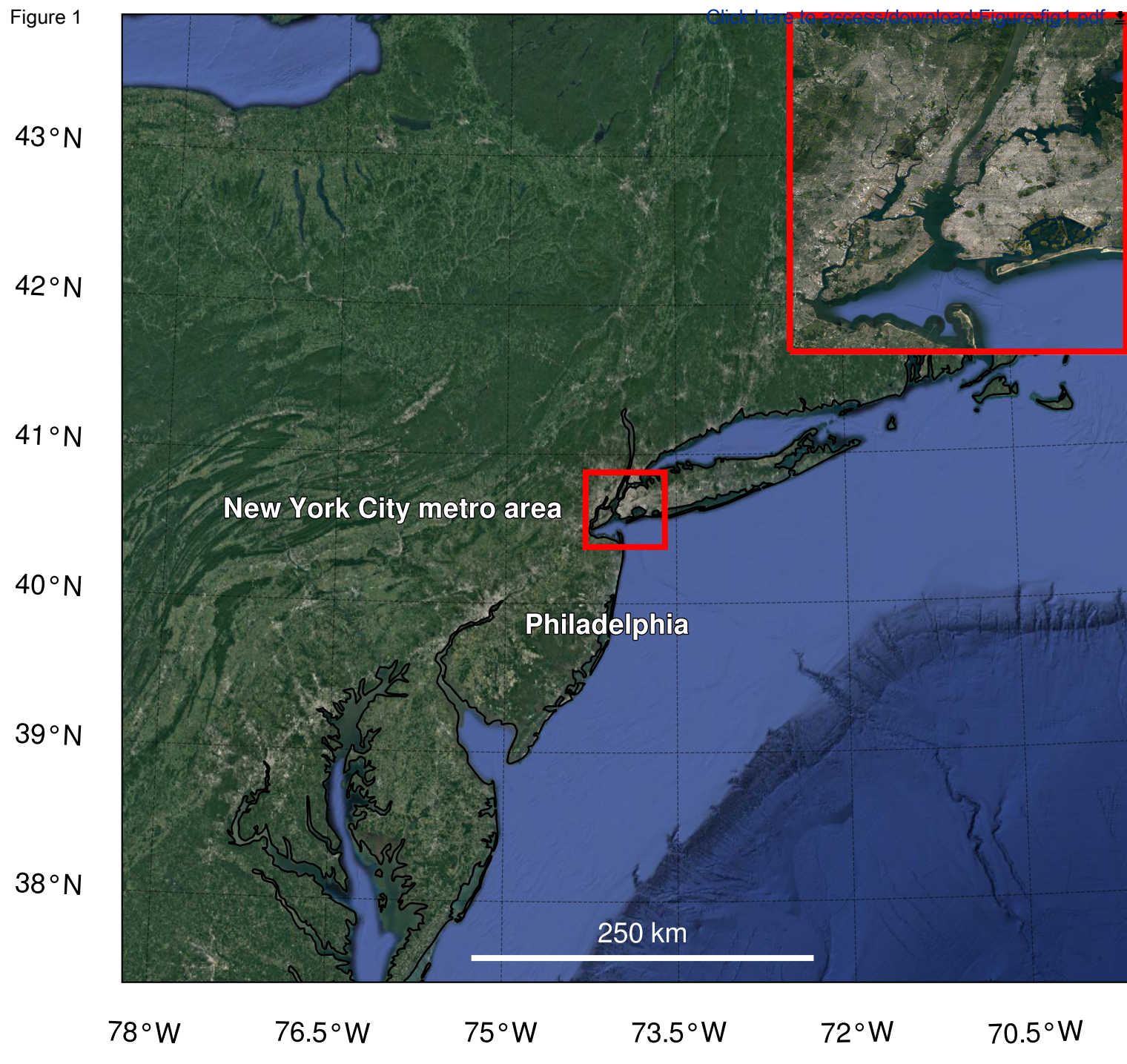


Figure 2

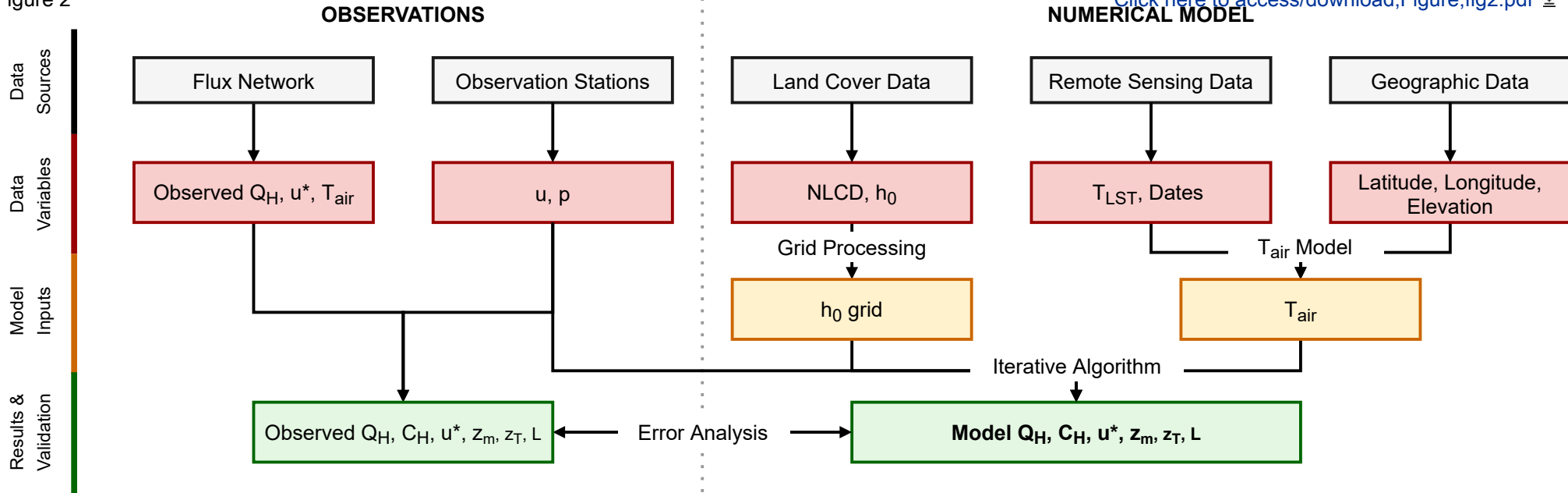
[Click here to access/download;Figure;fig2.pdf](#)

Figure 3



Flux Station

[Click here to access/download;Figure;fig3.pdf](#)

40.8°N

40.7°N

40.6°N

40.5°N

40.4°N

74.2°W

74.1°W

74°W

73.9°W

73.8°W

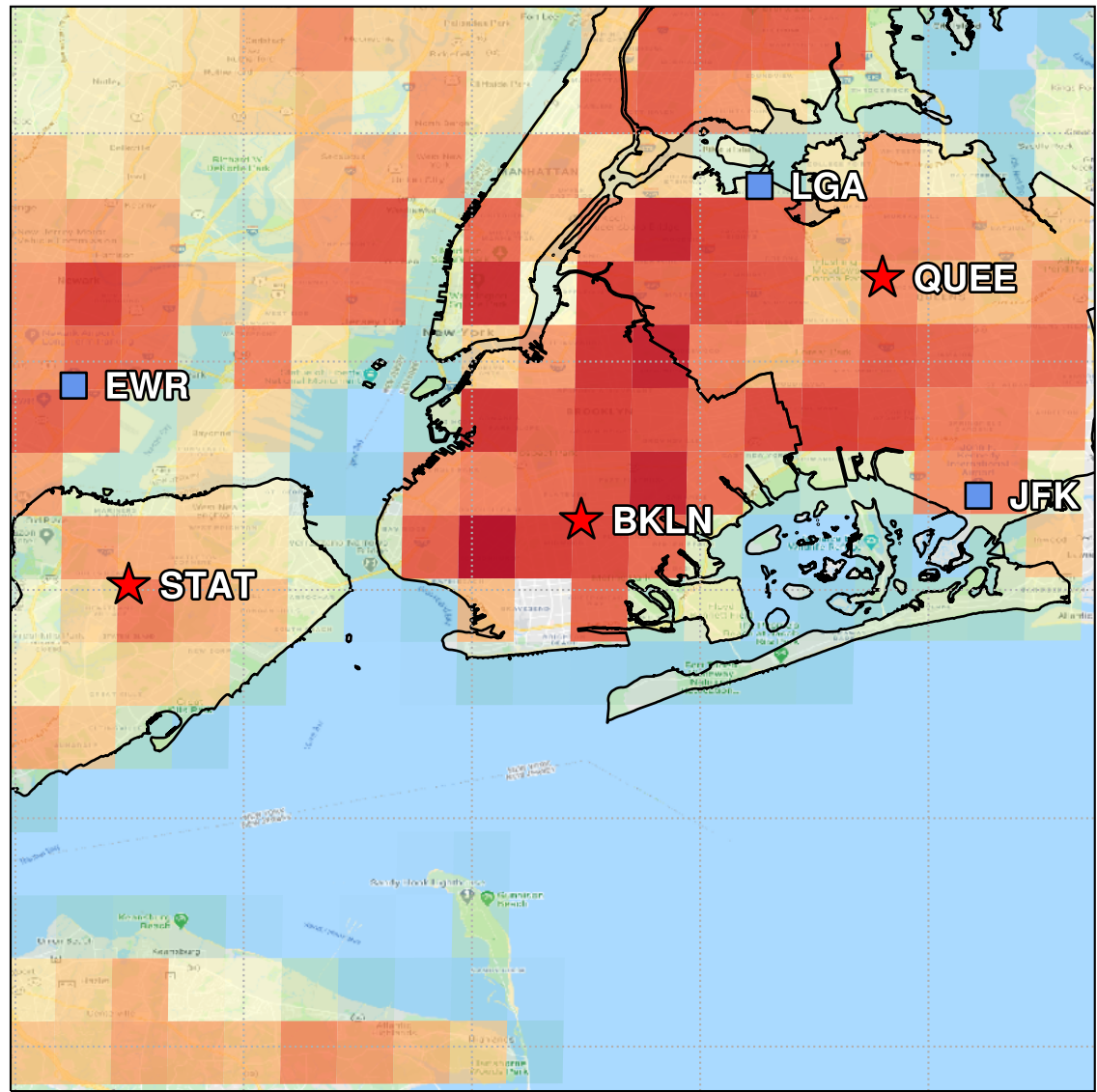


Figure 4

Number of data points
[Click here to access/download:Figure;fig4.pdf](#)

25 50 75 100 125 150 175

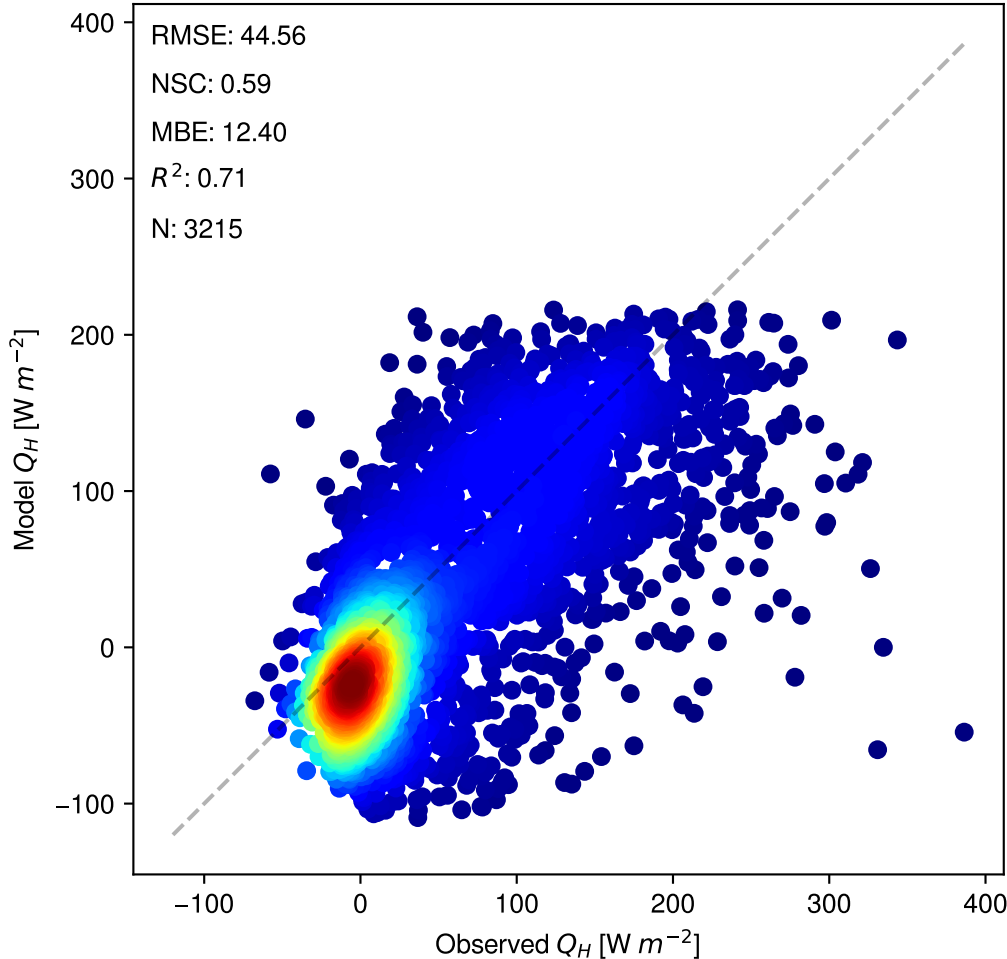


Figure 5

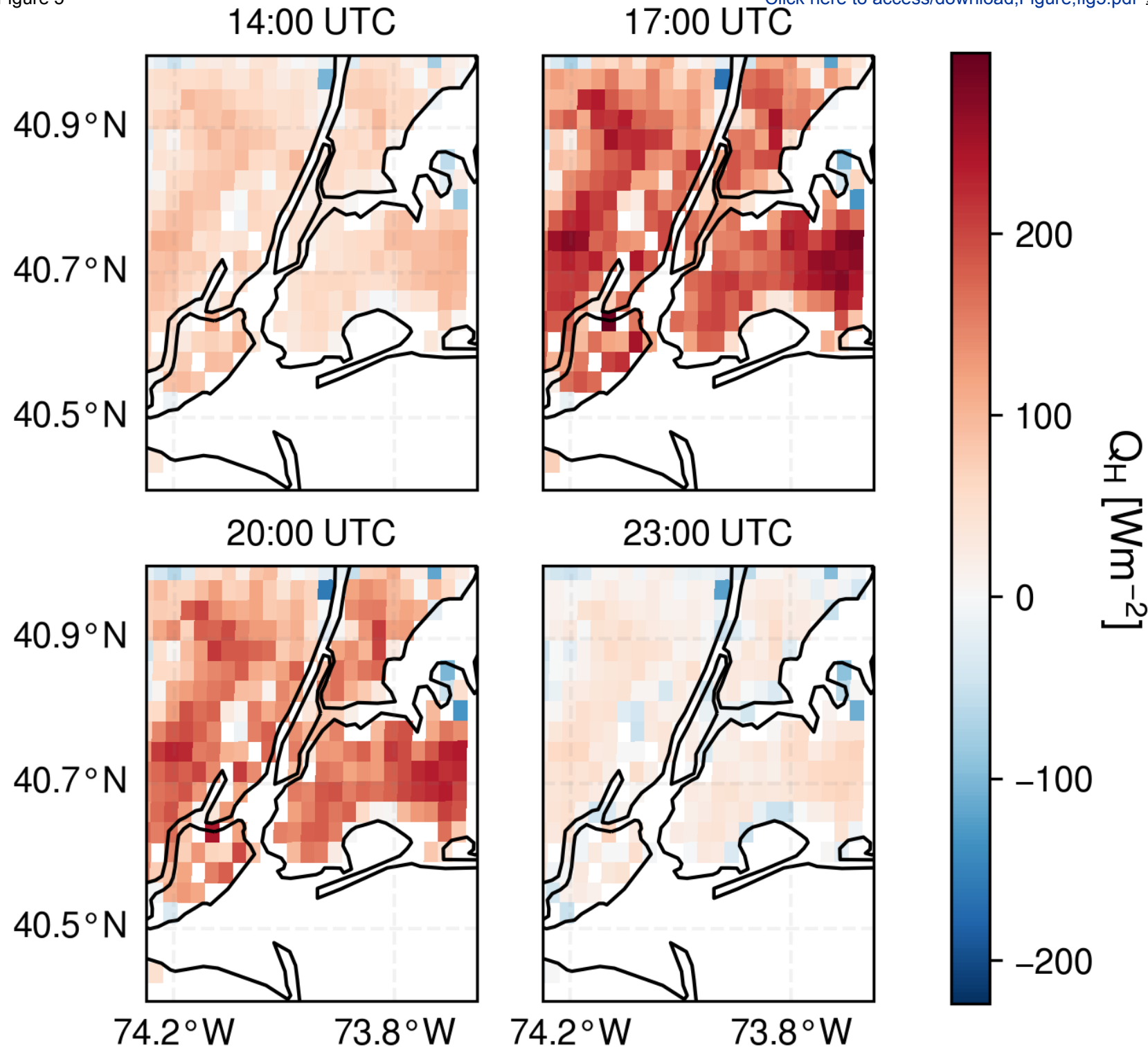
[Click here to access/download;Figure;fig5.pdf](#)

Figure 6

[Click here to access/download;Figure;fig6.pdf](#)

Number of data points

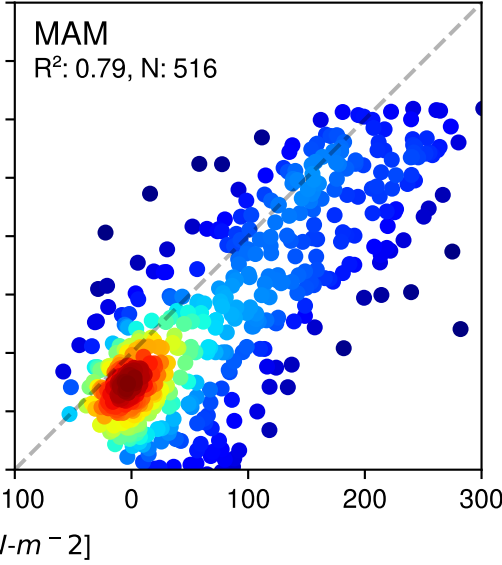
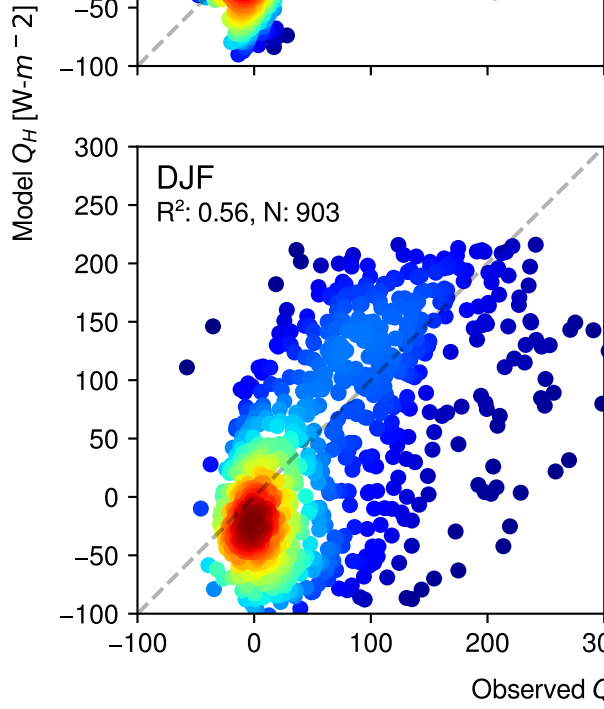
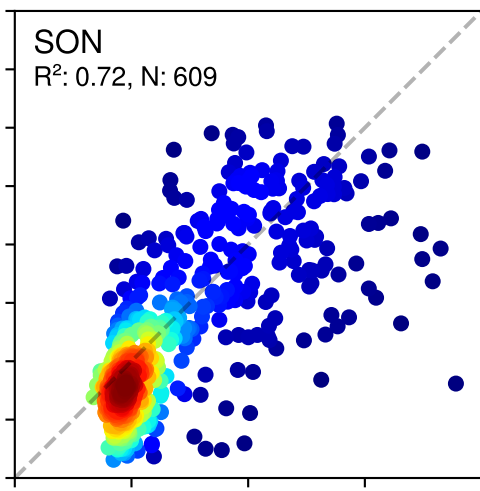
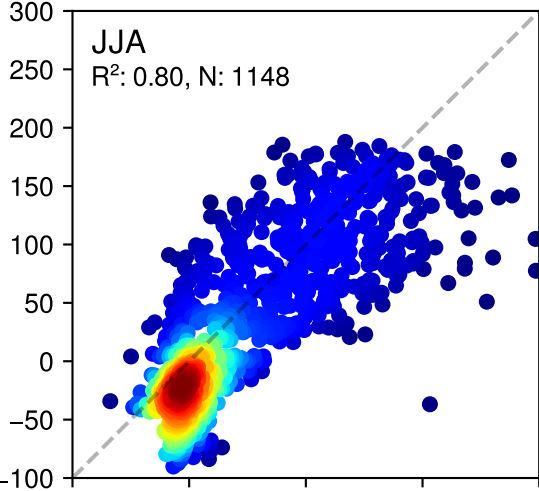


Figure 7a

Number of data points
[Click here to access/download;Figure;fig7a.pdf](#)

20 40 60 80 100 120 140 160

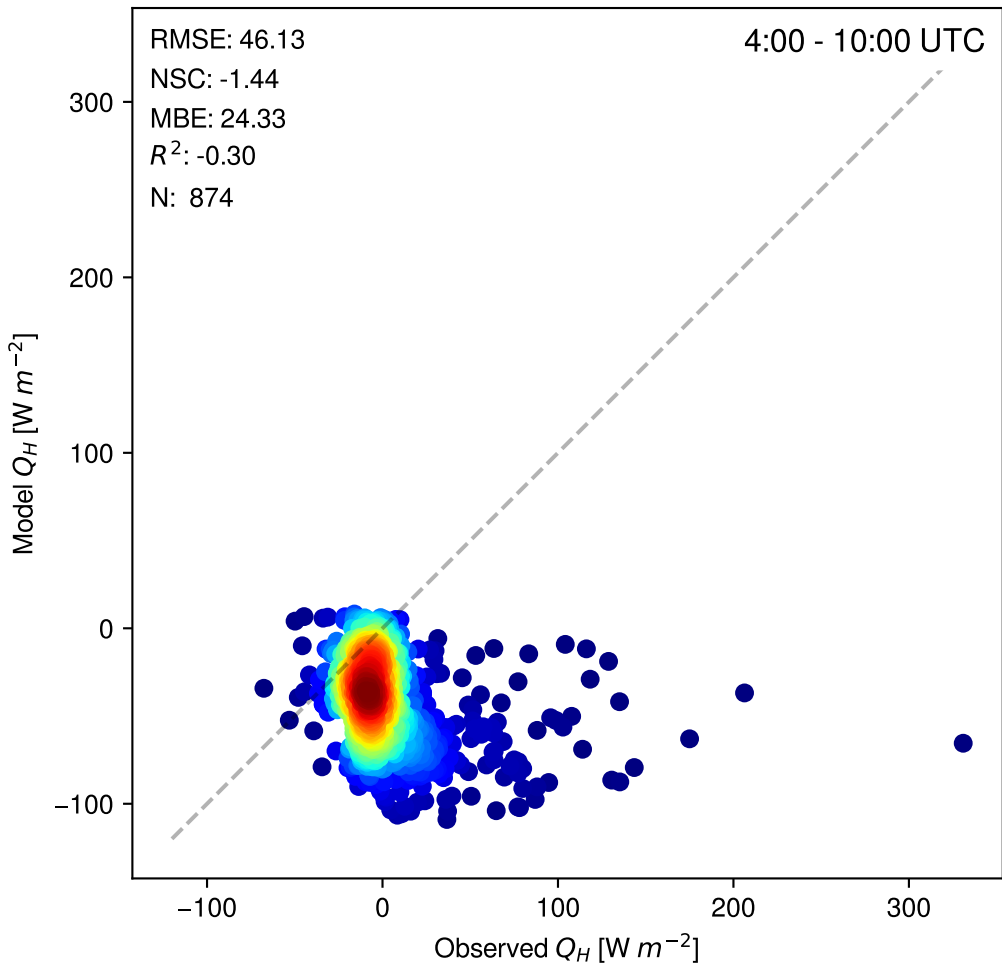


Figure 7b

Click here to
Number of data points
access/download;Figure;fig7b.pdf

5 10 15 20 25 30 35

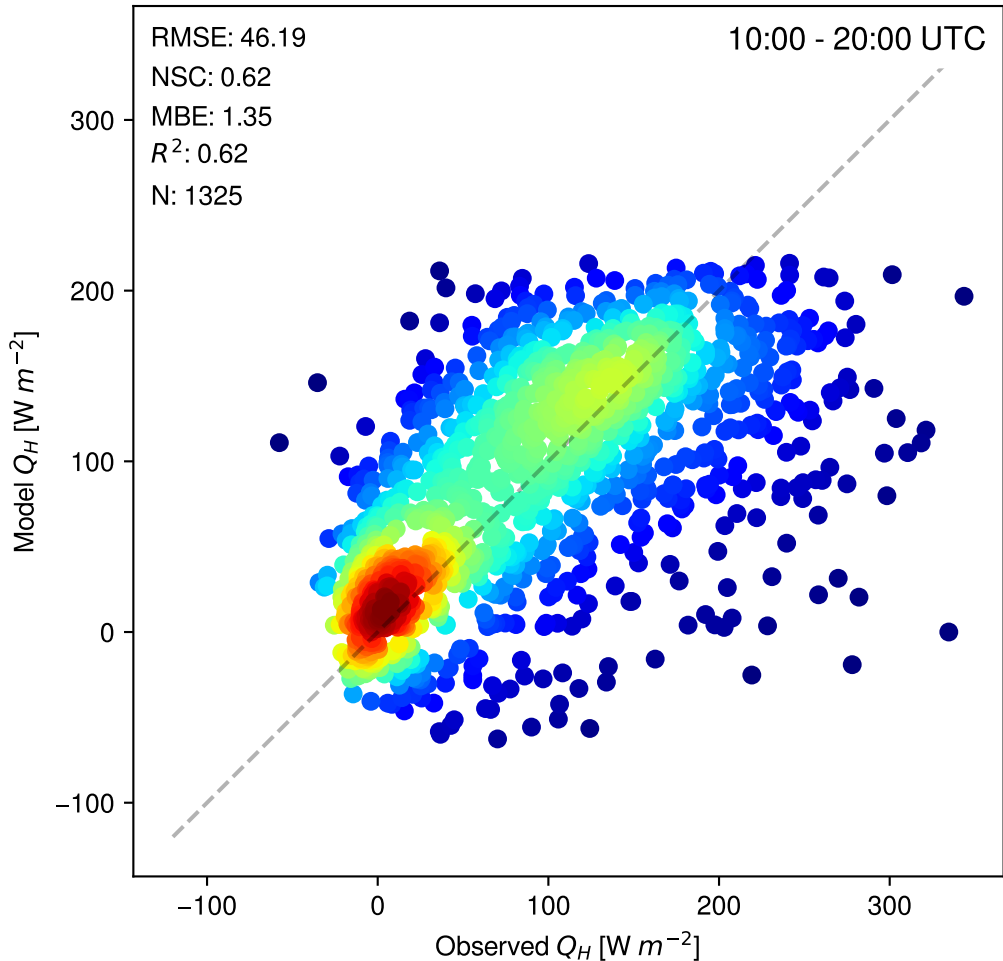


Figure 7c

Number of data points
[Click here to access/download: Figure; fig7c.pdf](#)

10

20

30

40

50

60

70

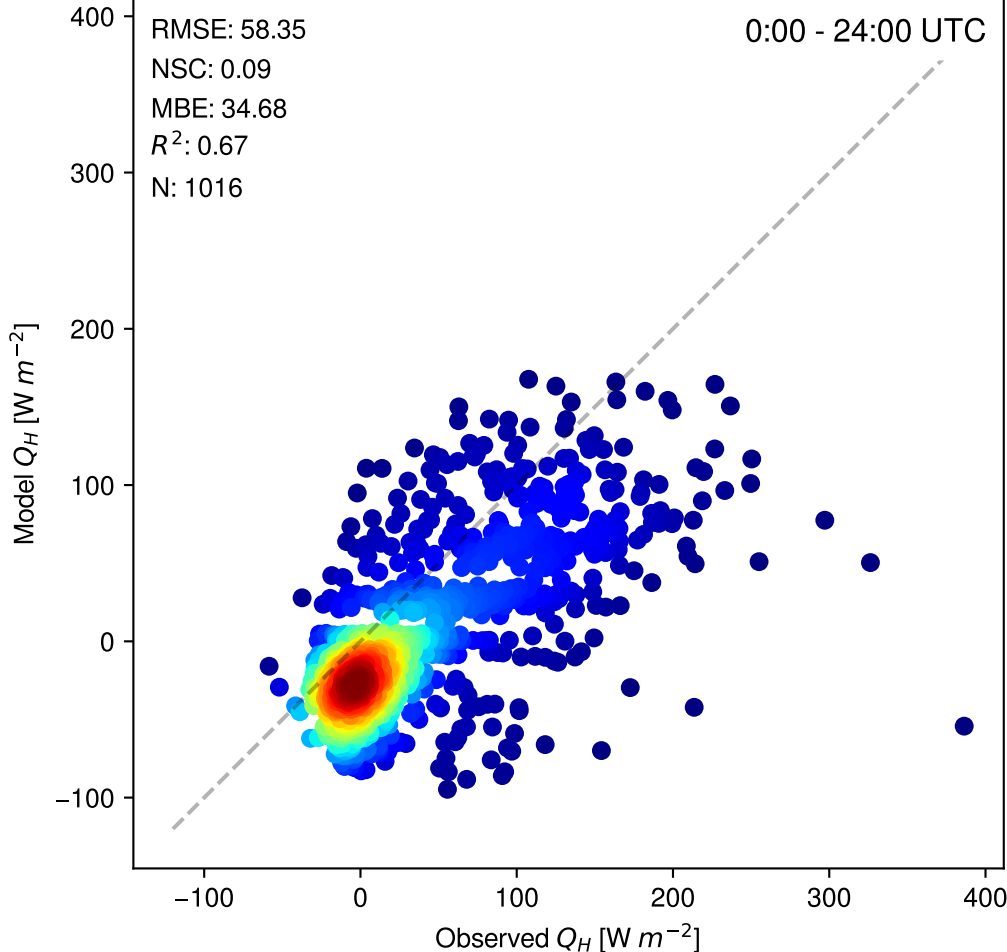


Figure 8

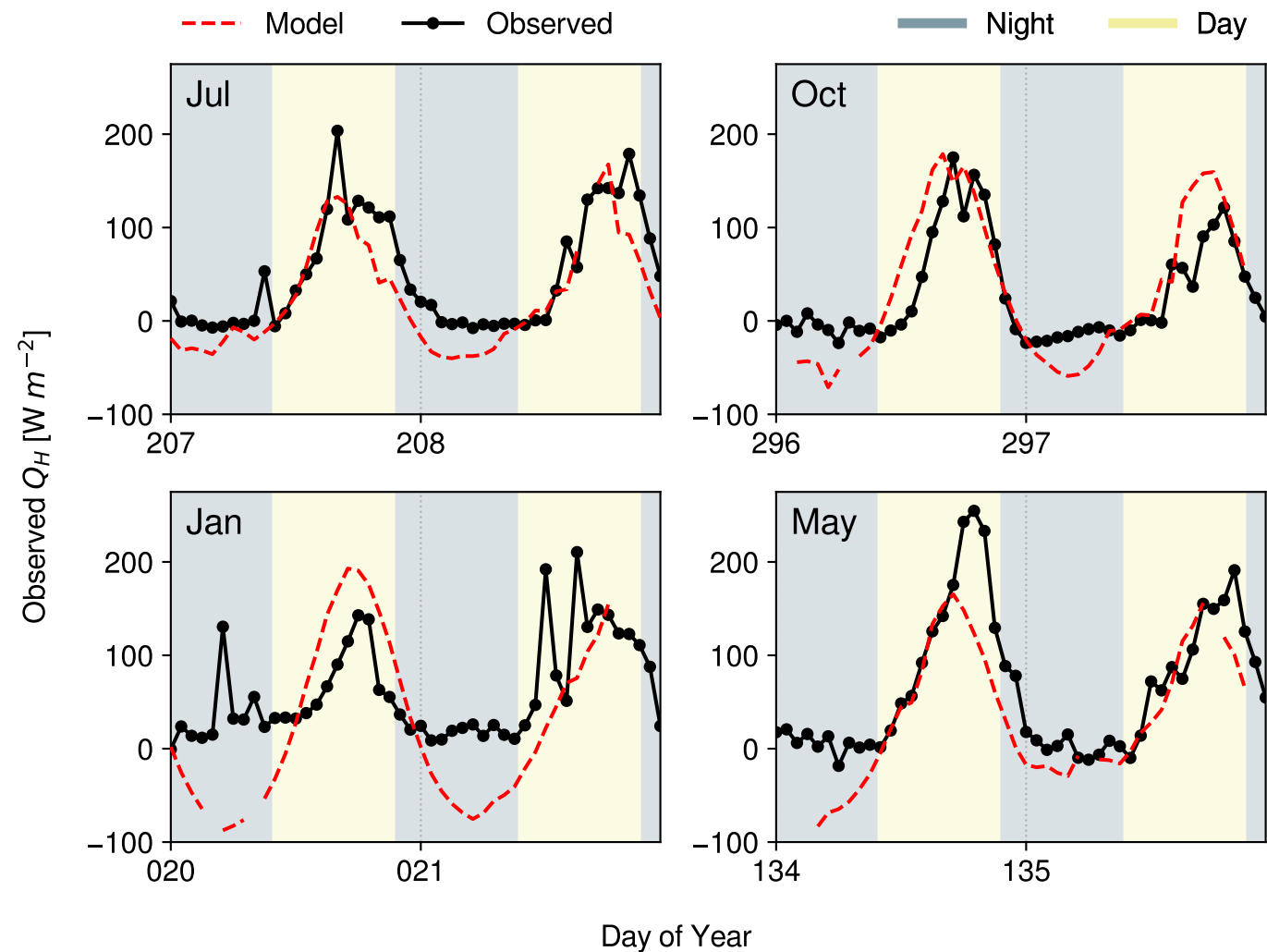
[Click here to access/download;Figure;fig8.pdf](#)

Figure 9

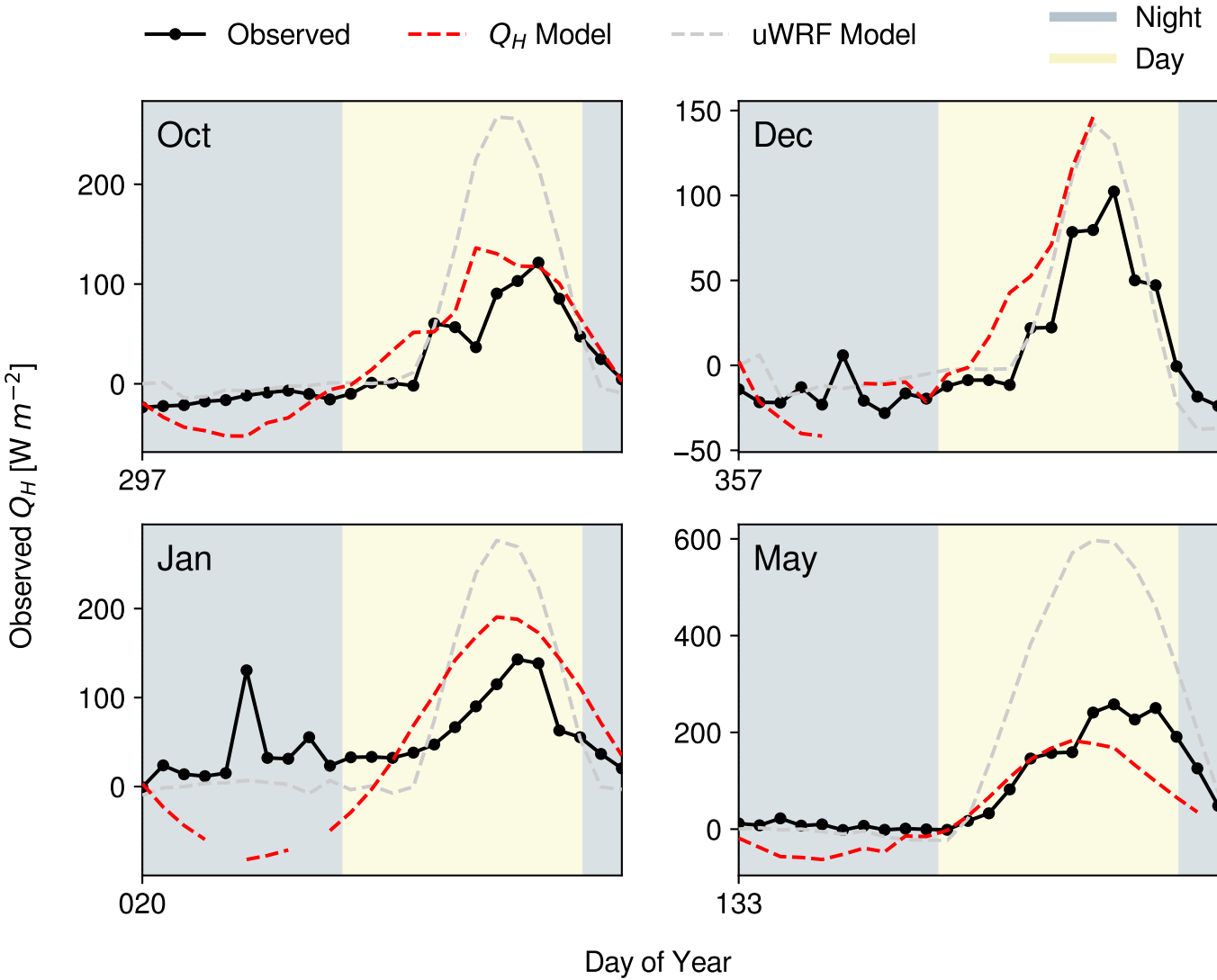
[Click here to access/download;Figure;fig9.pdf](#)

Figure 10a

2019-10-24 08:00:00

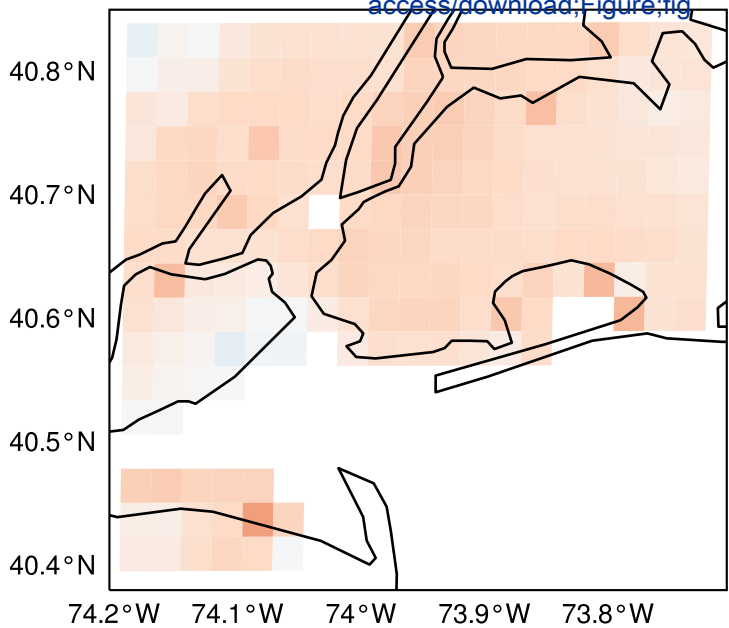
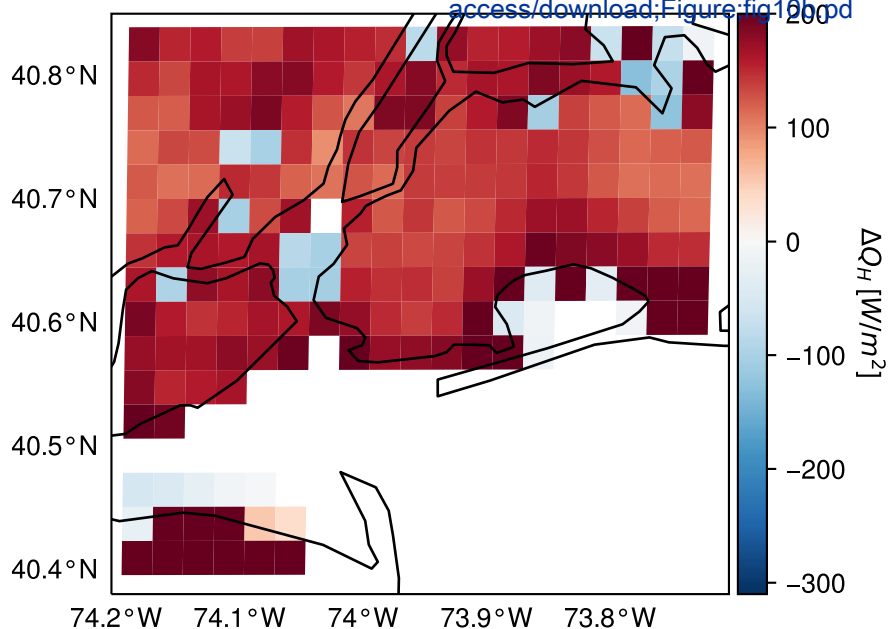
[Click here to
access/download;Figure;fig](#)

Figure 10b

2019-10-24 18:00:00

[Click here to
access/download; Figure:fig10b.pdf](#)

Declaration of interests

The authors declare that they have no known competing financial interests or personal relationships that could have appeared to influence the work reported in this paper.

The authors declare the following financial interests/personal relationships which may be considered as potential competing interests: